

Σ -nucleus potential studied with the (π^-, K^+) reaction on medium-to-heavy nuclear targets

P. K. Saha,^{1,*} H. Noumi,¹ D. Abe,² S. Ajimura,³ K. Aoki,¹ H. C. Bhang,⁴ K. Dobashi,² T. Endo,² Y. Fujii,² T. Fukuda,^{1,†} H. C. Guo,⁵ O. Hashimoto,² H. Hotchi,^{6,*} K. Imai,⁷ E. H. Kim,⁴ J. H. Kim,⁴ T. Kishimoto,³ A. Krutenkova,⁸ K. Maeda,² T. Nagae,¹ M. Nakamura,⁶ H. Outa,^{1,‡} T. Saito,⁹ A. Sakaguchi,³ Y. Sato,¹ R. Sawafta,¹⁰ M. Sekimoto,¹ Y. Shimizu,³ T. Takahashi,² H. Tamura,² L. Tang,¹¹ K. Tanida,^{6,‡} T. Watanabe,² H. H. Xia,⁵ S. H. Zhou,⁵ X. F. Zhu,⁵ and L. H. Zhu⁷

¹*IPNS, KEK, Tsukuba, Ibaraki 305-0801, Japan*

²*Department of Physics, Tohoku University, Sendai 980-8578, Japan*

³*Department of Physics, Osaka University, Toyonaka, Osaka 560-0043, Japan*

⁴*Department of Physics, Seoul National University, Seoul 151-742, Korea*

⁵*CIAE, P.O. Box 275-67, Beijing 102413, China*

⁶*Graduate School of Science, University of Tokyo, Tokyo 113-0033, Japan*

⁷*Department of Physics, Kyoto University, Kyoto 606-8532, Japan*

⁸*Institute of Theoretical and Experimental Physics, Moscow 117218, Russia*

⁹*Tohoku Gakuin University, Sendai 985-8537, Japan*

¹⁰*North Carolina A&T University, Greensboro, North Carolina 27411, USA*

¹¹*Department of Physics, Hampton University, Hampton, Virginia 23668, USA*

(Received 26 May 2004; published 29 October 2004)

In order to study the Σ -nucleus optical potential, we measured inclusive (π^-, K^+) spectra on medium-to-heavy nuclear targets CH₂, Si, Ni, In, and Bi. The CH₂ target was used to calibrate the excitation energy scale by using the elementary process $p + \pi^- \rightarrow K^+ + \Sigma^-$, where the C spectrum was also extracted. The calibration was done with ± 0.1 MeV precision. The angular distribution of the elementary cross section was measured and agreed well with the previous bubble chamber data, but with better statistics, and the magnitudes of the cross sections of the measured inclusive (π^-, K^+) spectra were also well calibrated. All of the inclusive spectra were found to be similar in shape at a region near to the Σ^- binding energy threshold, showing a weak mass-number dependence on the magnitude of the cross section. The measured spectra were compared with a theoretical calculation performed within the framework of the distorted-wave impulse approximation. It has been demonstrated that a strongly repulsive Σ -nucleus potential with a nonzero size of the imaginary part is required to reproduce the shape of the measured spectra.

DOI: 10.1103/PhysRevC.70.044613

PACS number(s): 21.80.+a, 25.80.Hp

I. INTRODUCTION

A hypernucleus is the result of implanting of a hyperon(s), such as Λ , Σ , Ξ , or $\Lambda\Lambda$, in an ordinary nucleus. Spectroscopic studies of hypernuclei can provide information on the hyperon behavior in a nucleus. One can learn about the hyperon-nucleon interaction and even the baryon-baryon interaction within the framework of SU_F(3) from the hypernuclear structure through the effective hyperon-nucleon interaction in a nucleus. So far, the spectroscopic studies of Λ hypernuclei are in a relatively advanced stage. The Λ major shell structures, even up to ${}^{89}_{\Lambda}\text{Y}$ or ${}^{208}_{\Lambda}\text{Pb}$, have been clearly observed with high-resolution spectroscopy in the (π^+, K^+) reaction [1–3], which have revealed the Λ single-particle nature. Namely, the binding energies of Λ can be well reproduced by a Woods-Saxon-type one-body potential [4]. In addition, high-resolution Ge detectors together with a magnetic

spectrometer have successfully observed γ transitions involving the Λ -hypernuclear states split by ΛN spin-dependent interactions, such as the spin-orbit and spin-spin forces in several light Λ hypernuclei [5,6].

On the other hand, knowledge about ΣN and Σ -nucleus interactions is still primitive, although the history of Σ -hypernuclear studies is almost comparable to that of Λ hypernuclei. Since a strong conversion process of Σ ($\Sigma N \rightarrow \Lambda N$) takes place inside a nucleus, the Σ -hypernuclear state is expected to be too broad to observe. The first claim of the observation of a narrow Σ -hypernuclear state by the Saclay-Heidelberg Collaboration [7] thus generated much experimental and theoretical excitement, but was excluded in the later experiment [8]. So far, many other experiments have been carried out on different light nuclear targets using the (K^-, π^{\pm}) reactions [9,10]. The only Σ -hypernuclear bound state has been established in ${}^4_{\Sigma}\text{He}$ produced by an in-flight (K^-, π^-) reaction on ${}^4\text{He}$ [9], which was first claimed at KEK [11]. The observation of this bound state was predicted with the effect of a strongly isospin-dependent Σ -nucleus potential (Lane term) [12]. The existence of the Lane term was also suggested in light nuclear systems from the systematic difference between the inclusive (K^-, π^{\pm}) spectra [10]. All of the other experiments could not find any bound

*Present address: Japan Atomic Energy Research Institute, Ibaraki 319-1195, Japan.

†Present address: Laboratory of Physics, Osaka E-C University, Neyagawa, Osaka 572-8530, Japan.

‡Present address: RIKEN, Wako, Saitama 351-0198, Japan.

Σ -hypernuclear state and failed to give any significant constraint on the Σ -nucleus potential. No data are available in heavier nuclei of $A > 16$. One may construct the Σ -nucleus folding potential based on the two-body hyperon-nucleon potentials. Unfortunately, the hyperon-nucleon potentials based on the one-boson-exchange model allow several sets of parameters, since hyperon-nucleon scattering data are very limited in accuracy as well as in statistical quality, as compared to the very precise data on the NN system. The information from the Σ^- -atomic data also leaves various shapes of possible potentials inside a nucleus, because the x-ray data are mainly sensitive to the potential outside the nucleus. Information concerning the Σ -nucleus potential can provide strong feedback not only in nuclear physics, but also in astrophysics. The role of strangeness in highly dense matter in a neutron star core is being intensively discussed [13–15]. The Σ^- interaction in nuclear matter is of particular importance, since Σ^- is expected to appear first in dense neutron matter to moderate the chemical potential while maintaining the charge neutrality due to its negative charge [15]. Therefore, new experimental data on medium heavy nuclei are desired in order to extract a conclusive understanding about the Σ -nucleus potential. Particularly, the central part of the Σ -nucleus potential is expected to be significant in heavy nuclei, where the Lane term is less dominant due to its A^{-1} dependence.

II. PRESENT EXPERIMENT

The present experiment (KEK-PS-E438) was carried out at the K6 beamline of the KEK 12-GeV proton synchrotron (PS) [16]. We measured inclusive (π^-, K^+) spectra for the first time on medium-to-heavy nuclear targets CH_2 , Si, Ni, In, and Bi. Since the inclusive (π^-, K^+) spectrum reflects the final-state interaction of a Σ^- with the residual nucleus, an analysis of the spectral shape would give the Σ -nucleus optical potential. The elementary reaction of



was measured with a CH_2 target in order to calibrate the energy scale and the cross section of the inclusive spectra. It is known that the elementary cross section at forward-scattering angles decreases rather smoothly with an increase of the incident-beam momentum, while the momentum transfer (Δp) increases rapidly below 1.2 GeV/ c [17]. A rapid change of Δp makes the spectrum analysis complicated and requires a wider momentum acceptance spectrometer system for the scattered kaon. The beam momentum was thus chosen to be 1.2 GeV/ c

III. EXPERIMENTAL SETUP

A schematic view of the whole experimental setup is shown in Fig. 1. It is composed of two parts: a beam spectrometer, used to measure the incident pion momentum, and the SKS system for the scattered kaon momentum. A detailed description of the spectrometer system can be found in Ref. [18].

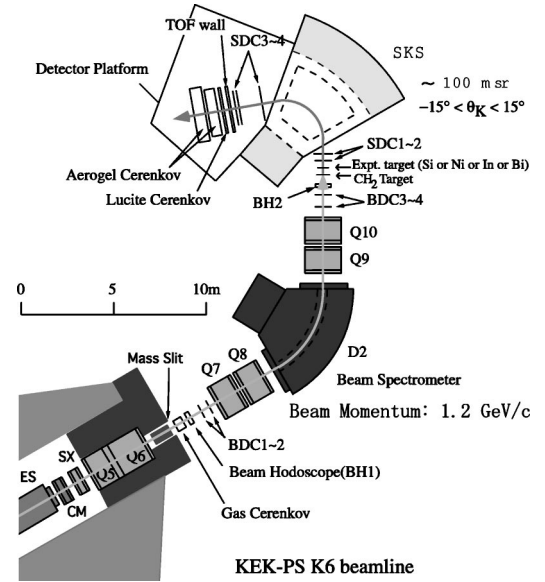


FIG. 1. Schematic view of the experimental setup.

A. Beam spectrometer

The beamline spectrometer comprises a dipole magnet and four quadrupole magnets (QQDQQ) together with four sets of high-rate drift chambers (BDC1–4), a freon-gas Čerenkov counter (eGC), and two sets of segmented plastic scintillation counters (BH1 and BH2). The electron contamination in the beam was rejected by eGC with a rejection efficiency better than 99.9%. The BH1 was segmented into seven vertical pieces of 5 mm thick and was installed downstream of eGC, while the BH2 was segmented into five vertical pieces of 3 mm thick. In order to reduce the energy-loss straggling in this counter, it was made as thin as possible and placed 40 cm upstream from the experimental target. The BH2 was used as a time-zero counter for timing measurements of incident and scattered particles. By requiring timing coincidence between BH1 and BH2, any contamination in the pion beam was rejected, where the beam trigger is defined as $\text{BEAM} \equiv \text{BH1} \times \text{BH2} \times \text{eGC}$.

The beamline drift chambers (BDC1–4) were placed upstream and downstream of the QQDQQ system. In order to operate under a high counting rate of several M/spill, the sense-wire spacing was made to be short (5 mm), where the drift space was ± 2.5 mm. Each chamber had six layers of sense-wire plane ($xx'uu'vv'$), where the vertical and $\pm 15^\circ$ tilted wire planes were denoted by x , u , and v , respectively. The beam track was measured by BDC's with a position resolution of 300 μm in rms. The beam momentum was obtained particle by particle by using a third-order transport matrix. In order to minimize the multiple-scattering effects on the momentum resolution, the QQDQQ system was designed so as to make the $\langle x | \theta \rangle$ term of the transport matrix to be zero between the focal planes close to the entrance and exit windows of 100- μm -thick stainless steel of the vacuum beam pipe and the drift chambers were made as thin as possible. The magnetic field of the dipole magnet (D2) was monitored throughout the experiment for every spill with a high-precision Hall probe in order to correct its fluctuation in the off-line analysis.

B. SKS spectrometer

The SKS spectrometer has a large acceptance of 100 msr, a good momentum resolution of 0.1% [full width at half maximum (FWHM)], and a linearity of within 0.1 MeV/c in its momentum acceptance of ±10% [18]. The SKS system is thus suitable to obtain high statistics over a wide excitation energy region with a good energy resolution, while maintaining the sensitivity of the imaginary part of the Σ-nucleus potential, because a bad resolution may cause the spectrum to smear out.

SKS comprises a superconducting dipole magnet together with four sets of drift chambers (SDC1–4) for momentum reconstruction and three kinds of trigger counters. The trigger counters comprise a scintillation counter wall (TOF), a lucite Čerenkov counter wall (LC), and two silica aerogel Čerenkov counters (AC1 and AC2) as seen in Fig. 1. The TOF counter comprised 15 vertical scintillation counters, each 7×100×3 cm³ in size, and was used for scattered-particle identification by measuring the time of flight from the reaction point. The LC was a threshold-type Čerenkov counter comprising 14 pieces of 10×140×4 cm³ Lucite radiators (*n*=1.49), which discriminated protons from pions and kaons. AC1 and AC2 were threshold-type silica aerogel Čerenkov counters (*n*=1.06) used to eliminate pions. The (π^-, K^+) trigger was defined as $PIK \equiv BEAM \times TOF \times LC \times AC1 \times AC2$. The trigger rate was typically 300 counts for a beam rate of 2.0×10^6 per spill.

The drift chambers SDC1 and SDC2 were installed at the entrance of the SKS magnet, while SDC3 and SDC4 were installed at the exit. SDC1 and SDC2 had the same drift-cell structure as the BDC's, as they were exposed to the beam. SDC3 and SDC4 had a large drift space of ±21 mm. The particle track with a position resolution of 300 μm was measured by SDC's.

In the present experiment, SKS was excited mainly to 272 A, which corresponds to 2.2 T, in order to measure the spectrum in the quasifree region covering partly below the Σ⁻ binding threshold. In addition, with Si and CH₂ targets, SKS was excited to two other different settings of 320 A (2.4 T) and 210 A (1.9 T) to measure the spectrum well below the Σ⁻ binding threshold and in the highly excited regions, respectively. The central momenta of SKS at 2.4 T, 2.2 T, and 1.9 T were 780 MeV/c, 720 MeV/c, and 620 MeV/c, respectively. The spectrum in one SKS setting could be connected smoothly to another as the acceptance regions partly overlap. The scattered-particle momentum was obtained particle by particle by reconstructing a particle trajectory with the Runge-Kutta tracking method using a precisely measured magnetic field map in each setting [19]. The magnetic field was monitored with an NMR probe throughout the data acquisition in order to correct its fluctuation in the off-line analysis. The fluctuation was as low as ±0.003%.

C. Experimental targets and data summary

In the present experiment we used CH₂ (1.00±0.05 g/cm²), Si (6.53±0.07 g/cm²), Ni (7.16±0.04 g/cm²), In (7.93±0.09 g/cm²), and Bi (9.74±0.10 g/cm²) of natural isotopic composition as ex-

TABLE I. Data summary of E438.

Target(s)	SKS current [Ap (T)]	Central momentum of SKS [MeV/c]	Irradiated π ⁻ [×10 ⁹]
CH ₂ and Si	210 (1.9)	630	86.5
CH ₂ and Si	272 (2.2)	720	228.7
CH ₂ and Si	320 (2.4)	780	101.6
CH ₂ and Ni	272 (2.2)	720	252.6
CH ₂ and In	272 (2.2)	720	352.3
CH ₂ and Bi	272 (2.2)	720	225.2
CH ₂ and Bi	272 (2.2)	720	120.7
CH ₂ only	272 (2.2)	720	47.3
CH ₂ only	272 (2.2)	720	39.4
Target empty	272 (2.2)	720	94.0

perimental targets. The quoted error on each target thickness came from a measurement. The thickness and the number of irradiated π⁻ on each target were optimized in order to obtain almost the same yield in the quasifree region for Σ⁻ production. The data were taken in two experimental cycles in 1999. Table I gives a data summary with specific SKS current settings according to the experimental requirement. The CH₂ target was always put in tandem at a distance of 250 mm upstream from other natural targets (Si or Ni or In or Bi), as demonstrated in Fig. 2. In order to calibrate the reliability of the vertical axis (cross section) throughout the experiment, as well as to obtain the energy resolution, the elementary $p(\pi^-, K^+)\Sigma^-$ process from the CH₂ target was used. On the other hand, the C spectrum was also extracted from the CH₂ target. The target empty data were used to check the background level in all inclusive spectra.

IV. DATA ANALYSIS

The hypernuclear mass (M_{HY}) in the (π^-, K^+) reaction was calculated by the following relation:

$$M_{HY} = \sqrt{(E_{\pi} + M_A - E_K)^2 - (p_{\pi}^2 + p_K^2 - 2p_{\pi}p_K \cos \theta_{\pi K})}, \quad (2)$$

where E_{π} and p_{π} are the total energy and momentum of a pion; E_K and p_K are those of a kaon. M_A is the mass of a target nucleus and θ is the scattering angle of the reaction.

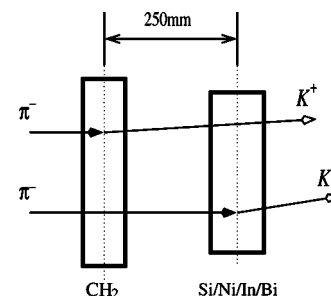


FIG. 2. Schematic view of the target configuration.

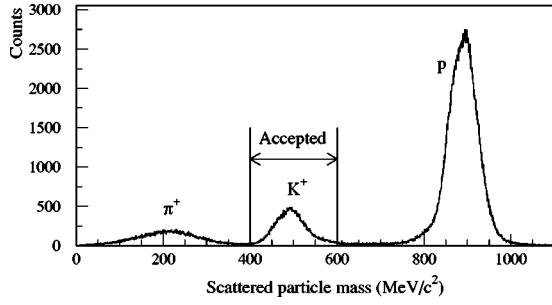


FIG. 3. Typical distribution of the scattered-particle mass obtained from the CH_2 and Si data. The gated region was used as good kaons.

The measured inclusive (π^-, K^+) spectra are presented as a function of the binding energy (B_{Σ^-}) of the Σ^- hyperon, which was defined as

$$B_{\Sigma^-} \equiv M_{A-1} + M_{\Sigma^-} - M_{HY}, \quad (3)$$

where M_{A-1} is the mass of a core nucleus at its ground state and M_{Σ^-} is the mass of a Σ^- hyperon.

A. (π^-, K^+) event selection and momentum reconstruction

The main background in the PIK trigger was fast protons that fired LC, while pions were well suppressed in the trigger level by AC1 and AC2. At the first stage of the off-line analysis, large background events in the PIK trigger were rejected by using only information from the counters. An incident π^- was selected from the time-of-flight information between BH1 and BH2, while the scattered K^+ was roughly selected from the analog-to-digital converter (ADC) and time-to-digital converter (TDC) information of the TOF and LC counters. Then, the π^- momentum and K^+ momentum were reconstructed from the track information of the BDC's and SDC's, respectively. In the tracking process, straight-line track candidates were first defined both at the entrance and exit of each spectrometer using a least-squares method. Then, the combination of the straight-line tracks that gave the least chi square in the momentum reconstruction was assigned as the best track candidate. In the beam spectrometer, a third-order transport matrix was used for momentum reconstruction, while in the SKS spectrometer the momentum was calculated by the Runge-Kutta method with a measured magnetic field map. After momentum reconstruction, the mass of a scattered particle was calculated as

$$M_{\text{scat}} = \frac{p}{\beta} \sqrt{1 - \beta^2}, \quad (4)$$

where β is the velocity of a scattered particle obtained from the time of flight and the flight path length between BH2 and TOF, and p is the reconstructed momentum. Figure 3 shows a typical mass spectrum of the scattered particles obtained from the CH_2 and Si data. Kaons were clearly identified separated from pions and protons, and the gated region was used as good events.

The scattering angle and the vertex point were obtained from the local straight track in BDC3 and BDC4 for the

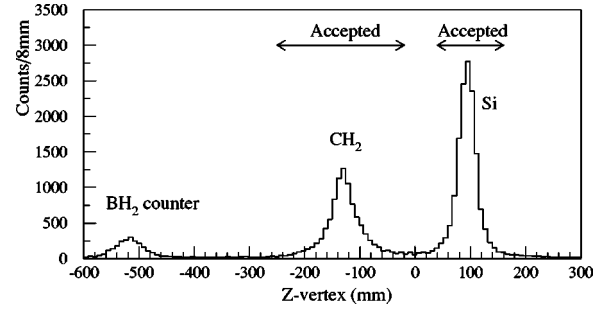


FIG. 4. Z-vertex distribution after selecting good kaons from the CH_2 and Si data.

incoming pion and a track obtained in the momentum reconstruction of the scattered particle in SKS. The Z axis was defined as the beam direction. Figure 4 shows a typical Z-vertex distribution from the CH_2 and Si data obtained by selecting good kaons, where events scattered in both targets as well as in the BH2 counter were clearly identified. However, the Z-vertex resolution at very forward-scattering angles was not good due to the multiple-scattering effects. A scattering angle (θ) cut greater than 4° was required to improve the Z-vertex resolution, as in Fig. 4. Two arrows indicated in Fig. 4 were the selected CH_2 and Si events used in the analysis.

B. Energy-scale calibration and energy resolution

The calibration of the horizontal axis (binding energy B_{Σ^-}) was one of the very important points of the present experiment, because the quasi free peak position of the inclusive spectrum is expected to provide information on the Σ^- -nucleus optical potential. Since the elementary, $p(\pi^-, K^+)\Sigma^-$ process from the CH_2 target was used for this purpose, the elementary peak stands at $259.177 \pm 0.029 \text{ MeV}/c^2$, which is the mass difference between a Σ^- and a proton [20]. The calibration process mainly consists of two parts (a detailed description can be found in Ref. [21]).

First, the energy losses of the incident pions and outgoing kaons in the target(s) were estimated from the beam through data taken with and without a target; second, correlations between the kaon momentum and the incident angles (horizontal and vertical) were needed to be solved so as to determine the SKS momentum offset value. This offset value should be kept the same for all sets of data in order to avoid any ambiguity in the calibration. Figure 5 shows a typical missing-mass spectrum from the CH_2 of CH_2 and Si data, where the kinematics was solved while considering the reaction with the proton target in CH_2 . The spectrum is plotted as a function of $M_{\Sigma^-} - M_p$ in MeV/c^2 at a scattering angle of $\theta_K = 6^\circ \pm 2^\circ$, where a calibration of the horizontal axis was not done. As a result, the elementary peak position was not found at the expected position ($259.177 \text{ MeV}/c^2$). A small satellite peak (left) came from events which did not pass through the downstream Si target, as can be seen from Fig. 2. A broad bump in the spectrum corresponds to the events from C in the CH_2 target. Two kinds of elementary events

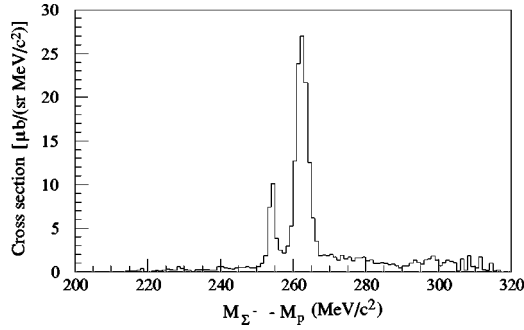


FIG. 5. Missing-mass spectrum of the (π^-, K^+) reaction from CH_2 in the proton-target kinematics before a horizontal-axis calibration. See text for details.

were identified in order to take into account the energy losses correctly. Figure 6 shows the horizontal axis corrected spectrum, where it was fitted with two Gaussians, as plotted with the solid curve. One Gaussian corresponds to the elementary peak, whereas the other one corresponds to the carbon contribution. From the fitting result, the elementary peak position was obtained at $259.23 \pm 0.13 \text{ MeV}/c^2$, as expected, whereas the energy resolution was obtained to be $3.31 \pm 0.33 \text{ MeV}$ (FWHM). The elementary peak position and the energy resolution were checked for all data sets (Table I), while keeping all of the offset parameters the same. An energy resolution of the spectrometer system is typically 2 MeV in FWHM, as achieved in the case of CH_2 only. The measured resolutions with the targets were consistent with those expected from the energy-loss straggling effects in the targets. A calibration of the horizontal axis was successfully achieved, as summarized in Table II, where the elementary peak position was always found to be the expected position within an error of $\pm 0.2 \text{ MeV}/c^2$. The error for the peak position in each data set came from the fitting result due to the statistical fluctuation.

The linearity of the SKS momentum was checked by passing an unscattered π^+ beam through the spectrometers without any target for several central beam momenta of

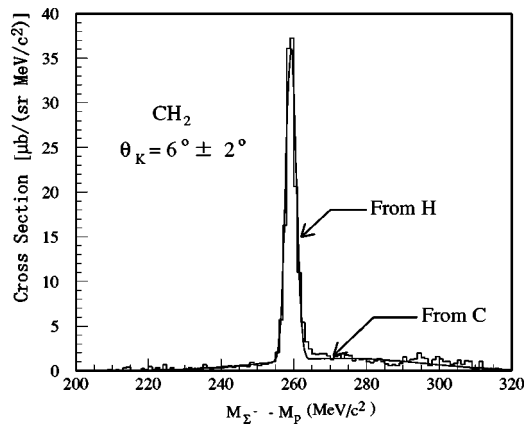


FIG. 6. Horizontal-axis corrected missing-mass spectrum for the elementary process from CH_2 , where the peak position is found at $259.23 \pm 0.13 \text{ MeV}/c^2$ with a resolution of $3.31 \pm 0.33 \text{ MeV}$ (FWHM). The expected peak position is at $259.177 \pm 0.029 \text{ MeV}/c^2$ the mass difference between a Σ^- and a proton [20].

TABLE II. Elementary $p(\pi^-, K^+)\Sigma^-$ peak position and the energy resolution after a horizontal axis calibration for all sets of data. The quoted errors are statistical.

Data set and SKS current	Elementary peak position (MeV/c^2)	Resolution (FWHM) (MeV)
CH_2 only (272 A)	259.20 ± 0.10	2.06 ± 0.20
CH_2 and Si (210 A)	259.23 ± 0.13	3.31 ± 0.33
CH_2 and Si (272 A)	259.27 ± 0.14	3.32 ± 0.29
CH_2 and Ni (272 A)	259.45 ± 0.19	4.44 ± 0.42
CH_2 and In (272 A)	259.39 ± 0.24	4.79 ± 0.50
CH_2 and Bi (272 A)	259.62 ± 0.26	5.16 ± 0.53

630–830 MeV/c , where the SKS was excited at 272 A. Here, we assumed that the central momentum of the beam spectrometer was exactly proportional to the magnetic fields of the beamline magnets. The linearity was found to be better than $\pm 0.072 \text{ MeV}/c$ in the momentum range [21].

C. Cross section

In order to obtain the cross section from the experimental yield, the experimental efficiencies and SKS acceptance were estimated. Then, the cross section was calculated as

$$\left(\frac{d\sigma}{d\Omega}\right) = \frac{A}{(\rho x)N_A} \frac{Y_K}{\sum_i I_i \epsilon_i} \sum_k \frac{1}{(\epsilon_{SDC12} \epsilon_{SDC34}) f_{decay} d\Omega(p, \theta)}, \quad (5)$$

where A is the target mass number, ρx the thickness of the target in g/cm^2 , N_A Avogadro's number, Y_K the yield number, I_i the number of irradiate π^- , and ϵ_i the several experimental and analysis efficiency factors: data-acquisition efficiency, BDC's efficiency, K6 tracking efficiency, beam-normalization factors, SKS tracking efficiency, Z-vertex cut efficiency, TOF and LC's efficiency, AC's accidental veto factor, and TOF and LC's multiplicity cut efficiency. ϵ_{SDC12} and ϵ_{SDC34} are the efficiencies of SDC12 and SDC34, respectively. These chambers had an incident position dependence of the efficiency, which was estimated event by event, as explained below. f_{decay} is the kaon decay rate and $d\Omega(p, \theta)$ the effective solid angle of SKS as a function of the kaon momentum and scattering angle.

1. Experimental and analysis efficiencies

The efficiencies mentioned above were estimated separately for all data sets. However, typical efficiencies obtained from the CH_2 and Si data with SKS at 272 A are described below.

The beam-normalization factor (f_{beam}) represents the fraction of π^- out of the total number of the beam (N_{beam}) and was estimated from the BEAM trigger events as $f_{beam} = (1 - f_\mu)(1 - f_{acc})$, where f_μ is the muon contamination in the π^- beam and f_{acc} is the accidental coincidence rate between BH1 and BH2. The e^- contamination was rejected by the good performance of eGC with an efficiency better than

99.9%. By requiring a good timing coincidence between BH1 and BH2, other contamination in the pion beam was rejected. However, muons in the beam that were the decay products of pions could not be separated from pions. We took this value from previous experiments, since it was studied and found to be 6.2% with a measurement error of $\pm 2.0\%$ for a $(1.0-1.10)\pi^+$ beam [22,23]. The factor f_{acc} was estimated as $(N_{beam}-N_{BH1,2})/N_{beam}$, where $N_{BH1,2}$ is the number of events for which the time of flight between BH1 and BH2 was proper for π^- . The factor f_{acc} was typically $4.4\% \pm 1.7\%$. Finally, the beam-normalization factor (f_{beam}) was found to be $89.6\% \pm 2.6\%$.

The BDC's efficiency was the total efficiency to obtain a straight track at the entrance and exit of the QQDQQ magnets, and was estimated to be $88.9\% \pm 1.6\%$, whereas the K6 tracking efficiency was the analysis efficiency to reconstruct a particle trajectory in the beam spectrometer, which was found to be $96.5\% \pm 1.4\%$.

In the analysis, more than two hits on TOF or LC were rejected in order to reduce the background level. The corresponding efficiency for this cut was estimated to be $98.7\% \pm 1.3\%$. The intrinsic efficiency of TOF and LC together was $99.6\% \pm 0.3\%$.

As a result of the high counting rate of AC1 and AC2, some of the PIK events were destroyed accidentally. The coincidence width between AC1, AC2, and BEAM \times TOF \times LC was 56 ± 5 ns, which was the dead time in the PIK trigger. The single counting rate of AC1 and AC2 was typically 1.5×10^5 s $^{-1}$. Thus, the AC's accidental veto factor (f_{AC}) was calculated to be $99.1\% \pm 0.2\%$.

The SKS χ^2 cut efficiency was estimated from the (π^-, p) events mixed in the PIK trigger. At first, a loose χ^2 cut was applied to reconstruct particle trajectories in SKS, and at the final stage of analysis a further tight cut was applied in order to reduce the background level as much as possible. The resolution in the particle identification was significantly improved by this cut, where the corresponding cut efficiency was estimated to be $92.2\% \pm 2.9\%$. The PID cut efficiency for kaons after the SKS χ^2 cut was found to be $99.4\% \pm 1.6\%$.

The Z-vertex resolution at very-forward-scattering angles was bad due to the multiple-scattering effect, as also mentioned earlier. In addition to the scattering angle cut ($>4^\circ$), tighter cuts were applied, as shown by the arrows in Fig. 4. The corresponding cut efficiencies were obtained by fitting the spectrum with a Lorentz function. Those were $90.0\% \pm 3.9\%$ and $92.2\% \pm 2.8\%$ for CH₂ and Si, respectively in the CH₂ and Si data.

The efficiency of SDC1 and SDC2 (ϵ_{SDC12}) was the total efficiency, including the analysis efficiency, and was estimated using the BEAM trigger. In SDC1 and SDC2, the beam-counting rate per wire was quite high because the beam was focused at a target. As a result, a small degradation of the efficiency near the beam spot was observed. Therefore, the efficiency was estimated as a function of the horizontal incident position for the event-by-event correction. The average efficiency of SDC1 and SDC2 was typically $92.8\% \pm 1.2\%$.

The efficiency of SDC3 and SDC4, including the analysis efficiency, was estimated from the (π^-, p) events. Since it

had an incident position dependence of the efficiency due to some noisy channels, the efficiency as a function of the horizontal incident position was used for corrections event by event, where the average value of the SDC3 and SDC4 efficiency was found to typically be $85.2\% \pm 1.7\%$.

2. Other factors

The data-acquisition efficiency is caused by the dead time of the data-acquisition system. It was estimated from the ratio of the number of events accepted by the data-acquisition system to that of triggers and was typically $80.4\% \pm 0.1\%$.

The kaon decay rate in SKS was studied in detail with a Monte Carlo simulation by Hasegawa [22]. The corresponding correction factor was typically $40.0\% \pm 2.0\%$ and was corrected event by event while taking into account the momentum and the flight path length.

3. SKS acceptance

The acceptance of the SKS spectrometer to obtain the effective solid angle ($d\Omega$) was calculated by a Monte Carlo simulation code GEANT [24]. The geometrical condition of the experiment, the effect of the energy loss, the multiple-scattering effect, and the off-line analysis cut condition were taken into account. In addition, a timing cut at the lower-momentum side of the TOF wall was applied, as it was found by comparing the timing spectra from the simulation and the data [21]. In the event generator, the distribution of the beam profile obtained from the experimental data was produced and the effective solid angle was averaged on the distribution. It was calculated as a function of the scattering angle (θ) and momentum (p), as follows:

$$d\Omega(p, \theta) = \int_{\theta-(1/2)\Delta\theta}^{\theta+(1/2)\Delta\theta} d \cos \theta \int_0^{2\pi} d\phi C(p, \theta), \quad (6)$$

where $C(p, \theta)$ is the ratio of the accepted events to the generated events. The events were generated uniformly from $\theta - \frac{1}{2}\Delta\theta$ to $\theta + \frac{1}{2}\Delta\theta$ in the polar angle, from 0 to 2ϕ in the azimuthal angle, and from $p - \frac{1}{2}\Delta p$ to $p + \frac{1}{2}\Delta p$ in the momentum.

D. Elementary $p(\pi^-, K^+)\Sigma^-$ cross section

Taking into account all of the above-mentioned efficiencies and the SKS acceptance, the differential cross section at the kaon scattering angle of $6^\circ \pm 2^\circ$ in the laboratory frame was obtained as follows:

$$\left(\frac{d\sigma}{d\Omega}\right)_{4^\circ-8^\circ} \equiv \int_{\theta=4^\circ}^{\theta=8^\circ} \left(\frac{d\sigma}{d\Omega}\right) d\Omega \bigg/ \int_{\theta=4^\circ}^{\theta=8^\circ} d\Omega. \quad (7)$$

Data from the elementary process in the present experiment were used mainly to calibrate the excitation energy scale as well as to check the accuracy of the measured cross section. The calibration of the energy scale has already been described earlier. The elementary cross sections obtained from all sets of data are presented in this section. In Fig. 6, the vertical axis is calibrated to be the cross section in units of

TABLE III. Elementary $p(\pi^-, K^+)\Sigma^-$ cross section from different sets of data. The quoted errors are both statistical (stat) and systematic (syst).

Data set and (SKS current)	$\left(\frac{d\sigma}{d\Omega}\right)_{\pi^-p \rightarrow \Sigma^-K^+}^{4^\circ-8^\circ}$ [$\mu\text{b}/\text{sr}$]
CH ₂ only (272 A)	127.20±9.59(stat)±7.19(syst)
CH ₂ and Si (210 A)	128.41±8.13(stat)±6.09(syst)
CH ₂ and Si (272 A)	124.73±7.48(stat)±6.15(syst)
CH ₂ and Ni (272 A)	127.46±6.52(stat)±8.51(syst)
CH ₂ and In (272 A)	122.82±5.42(stat)±6.54(syst)
CH ₂ and Bi (272 A)	123.98±5.14(stat)±7.02(syst)

$\mu\text{b}/(\text{sr MeV}/c^2)$. By subtracting the carbon contribution, the elementary cross section was extracted from the proton peak and was found to be $128.41 \pm 8.13(\text{stat}) \pm 6.09(\text{syst}) \mu\text{b}/\text{sr}$. The quoted errors are statistical (stat) and systematic (syst), respectively. Elementary cross sections obtained from all sets of data are summarized in Table III along with both the statistical and systematic errors. The elementary cross section was found to be consistent in each set of data within the errors. This demonstrates the stability of estimating the SKS acceptance as well as all of the detectors and analysis efficiencies during the experiment.

The angular distribution of the elementary cross section was obtained over a wide angular range from the CH₂ and Si data with SKS at 210 A. Only this setting could well cover the kaon momentum over a wider angular range. In Fig. 7, the obtained angular distribution is shown by open circles, where the two cross points are those from old bubble-chamber data measured at a beam momentum of 1.225 GeV/c [25]. The past data were originally reported in the center-of-mass system. They were transferred to the laboratory system in order to compare them with the present

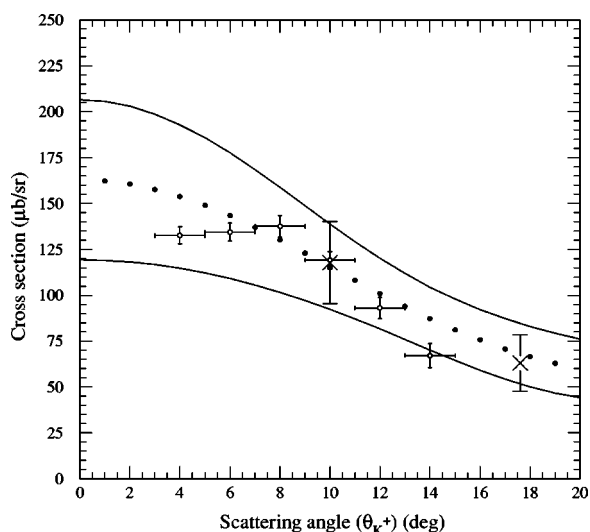


FIG. 7. Angular distribution of the elementary reaction in the laboratory system. The open circles are the present measurement, where the crosses are from previous bubble-chamber data [25]. See the text for details. The quoted errors are statistical.

result and two data points were found at $\theta_K=10^\circ$ and 17.5° . The dotted curve was obtained by fitting the previous data with a Legendre function, where the solid lines show the error boundaries. The present measurement agrees well with the previous one with better statistics.

E. Systematic errors

In order to obtain the total systematic errors of the cross section, the measurement error of the target thickness, the SKS acceptance, and the incident-position-dependent efficiencies of SDC12 and SDC34 were taken into account. The effects of other sources were found to be very small, so as to be negligible. The efficiencies of SDC12 and SDC34 varied with the position. Particularly, SDC34 had a significant inefficiency for some channels at the lower-momentum side. In order to obtain systematic errors, the efficiency functions of SDC12 and SDC34 were varied within the fitting errors [21]. The SKS acceptance was also found to be affected at the lower-momentum side due to the trigger timing problem, as also mentioned earlier. To study the systematic error, the SKS acceptance was recalculated by changing the TOF timing cut within the typical time resolution of the TOF counter. The total systematic errors obtained for the elementary cross section are summarized in Table III. The systematic errors in the inclusive spectra were found to be larger in the higher-excitation-energy region as compared to the lower-excitation-energy region, because the systematic errors were mainly affected at the lower-momentum side.

F. Background level

One of the main advantages of the (π^-, K^+) reaction over the (K^-, π^\pm) reactions is its low-background nature. To examine the background level exactly, in addition to the data on nuclear targets, some data were taken without any target, as shown in Table I, where the SKS current setting was at 272 A in order to see the background level mostly near to the Σ^- binding energy threshold. The target-empty data were analyzed using the same analysis program and conditions as that for the normal data. The background level was found to be very low, as can be seen in Fig. 8 (dashed line histogram). The solid line histogram was the (π^-, K^+) spectrum from the Si target. The horizontal axis is the binding energy of Σ^- ($-B_{\Sigma^-}$), whereas the vertical axis shows the counts. The total entries are 7655 and 26 for Si and target-empty data, respectively, where the number of π^- irradiations for target-empty data was about half the amount compared to that for the Si target. For a comparison, the vertical axis was normalized by the total number of the beam (N_{π^-}) for each case. As can be seen, the background was found to be almost uniform, about two orders of magnitude lower than the spectrum with the target, and there was no background event around the bound region. Thus, we neglected the background in analyzing the inclusive spectra for all of the targets.

V. EXPERIMENTAL RESULTS

The inclusive (π^-, K^+) spectra at a scattering angle of $6^\circ \pm 2^\circ$ on Si, C, Ni, In, and Bi are presented here. The dif-

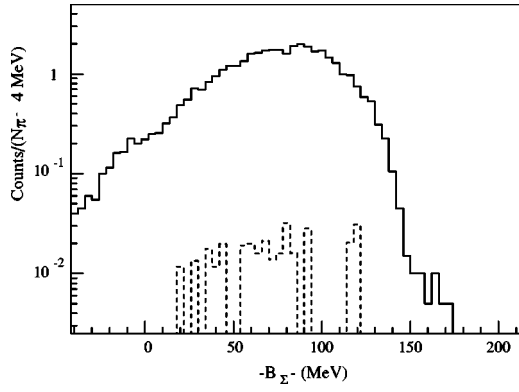


FIG. 8. Background level in the (π^-, K^+) reaction from the target-empty data analysis. The horizontal axis shows the binding energy of a Σ^- , whereas the vertical axis shows the counts. The solid-line histogram is from the Si target, while dashed-line histogram is from the target-empty runs.

ferential cross section was obtained by Eq. (7). All of the inclusive spectra are also presented in the tabular form in Tables IV–VIII.

A. Si spectrum

Figure 9 shows the inclusive (π^-, K^+) spectra on Si obtained from three data sets of CH_2 and Si with three SKS current settings. The horizontal axis is the missing mass in terms of $-B_{\Sigma^-}$, and the vertical axis is the differential cross section in $\mu\text{b}/(\text{sr MeV})$. Three spectra from three settings were found to be matched very well for the overlap region of the acceptance. These three settings together cover a wide energy region so as to understand the gross feature of the whole spectral shape. By taking a weighted average from three spectra, the combined Si spectrum is shown in Fig. 10, where the spectrum has been shown in both statistical and systematic errors. A small amount of CH_2 contamination found in the Si spectrum was subtracted with a proper scale. The CH_2 contamination was found in all inclusive spectra and was subtracted in the same manner [21]. As can be seen in the figure, the cross section was found to gradually increase with an increase of $-B_{\Sigma^-}$, and the maximum was around $-B_{\Sigma^-}=120$ MeV. There is also a significant yield found below the binding energy threshold.

B. C spectrum

The inclusive (π^-, K^+) spectrum on C was extracted from the CH_2 data. Like the Si spectrum, the C spectrum was also taken with three SKS settings and was found to be matched well. The averaged C spectrum is shown in Fig. 11. The sudden gap in the spectrum at around 100 MeV was due to removing a sharp peak in the CH_2 data, which included both H and C events; C events were very hard to separate. Nevertheless, we can fairly well discuss the spectrum from a deeply bound region to around 80 MeV above the Σ^- binding threshold.

TABLE IV. Inclusive (π^-, K^+) spectrum on Si as a table. The quoted values of $-B_{\Sigma^-}$ are at the center of bins.

$-B_{\Sigma^-}$ (MeV)	$\bar{\sigma}_{4^\circ-8^\circ}$ ($\mu\text{b}/\text{sr}/\text{MeV}$)	Statistical errors	Systematic errors
-50.0	0.0308	0.0127	0.0006
-46.0	0.0174	0.0109	0.0008
-42.0	0.0184	0.0108	0.0003
-38.0	0.0223	0.0115	0.0015
-34.0	0.0375	0.0135	0.0015
-30.0	0.0280	0.0126	0.0005
-26.0	0.0292	0.0113	0.0010
-22.0	0.0503	0.0133	0.0007
-18.0	0.0410	0.0121	0.0005
-14.0	0.0498	0.0126	0.0012
-10.0	0.0598	0.0123	0.0008
-6.00	0.0576	0.0130	0.0010
-2.00	0.0635	0.0136	0.0018
2.000	0.0644	0.0133	0.0032
6.000	0.0804	0.0158	0.0036
10.00	0.0908	0.0147	0.0010
14.00	0.1129	0.0160	0.0087
18.00	0.1335	0.0161	0.0020
22.00	0.1556	0.0172	0.0092
26.00	0.1831	0.0183	0.0039
30.00	0.1974	0.0188	0.0038
34.00	0.2201	0.0192	0.0031
38.00	0.2667	0.0206	0.0039
42.00	0.3287	0.0227	0.0054
46.00	0.3741	0.0241	0.0078
50.00	0.4054	0.0255	0.0200
54.00	0.4594	0.0267	0.0126
58.00	0.5491	0.0287	0.0117
62.00	0.5667	0.0292	0.0100
66.00	0.6636	0.0329	0.0116
70.00	0.7360	0.0352	0.0143
74.00	0.7952	0.0372	0.0144
78.00	0.8061	0.0380	0.0140
82.00	1.0008	0.0448	0.0187
86.00	1.0527	0.0472	0.0271
90.00	1.0397	0.0496	0.0472
94.00	1.1750	0.0594	0.0280
98.00	1.2382	0.0719	0.0251
102.0	1.2491	0.0629	0.0261
106.0	1.1228	0.0564	0.0233
110.0	1.3462	0.0649	0.0311
114.0	1.3898	0.0662	0.0386
118.0	1.3375	0.0674	0.0712
122.0	1.3845	0.0746	0.0842
126.0	1.5055	0.0789	0.0635
130.0	1.4338	0.0788	0.0514
134.0	1.3521	0.0902	0.1235

TABLE IV. (Continued.)

$-B_{\Sigma^-}$ (MeV)	$\bar{\sigma}_{4^\circ-8^\circ}$ ($\mu\text{b}/\text{sr}/\text{MeV}$)	Statistical errors	Systematic errors
138.0	1.3523	0.0919	0.1005
142.0	1.3539	0.0950	0.0898
146.0	1.4285	0.1075	0.0842
150.0	1.4456	0.1171	0.1201
154.0	1.4067	0.1179	0.0751
158.0	1.3604	0.1227	0.1016
162.0	1.4187	0.1283	0.1731
166.0	1.3470	0.1384	0.1146
170.0	1.6948	0.1666	0.1028
174.0	1.3139	0.1550	0.1028
178.0	1.2560	0.2420	0.0461
182.0	1.5632	0.2263	0.0946
186.0	2.0955	0.3099	0.0765
190.0	0.8844	0.2094	0.5393
194.0	0.9897	0.5720	0.3064
198.0	0.4460	0.3163	0.1451
202.0	1.1287	0.5051	0.2822
206.0	0.2095	0.1489	0.7257
210.0	0.3247	0.2302	0.1518

C. Ni, In, and Bi spectra

Inclusive spectra on Ni, In, and Bi were taken only at an SKS current setting of 272 A, which are shown in Figs. 12–14, respectively.

D. Similarity of the spectra

From an analysis of all the inclusive spectra, it was found that all spectra show a similarity in shape at least up to $-B_{\Sigma^-}=90$ MeV, as shown in Fig. 15. All spectra with only an SKS setting of 272 A were used to make the comparison fair.

1. Mass-number dependence of the cross section

The mass-number dependence of the Σ^- production cross section was obtained from the ratio of the inclusive Si spectrum to that of the others. The ratios were simply taken bin by bin at an energy region of $0 < -B_{\Sigma^-} < 90$ MeV. The ratios were found to be very flat over the energy region and were fitted by a straight line. The fitting results are summarized in Table IX.

2. Comparison of the mass-number dependence to the eikonal approximation

The effective nucleon number (N_{eff}) of the (π^-, K^+) reaction on C, Si, Ni, In, and Bi at 6° was calculated by the eikonal approximation. A brief description of the calculation is given in Ref. [21].

The mass-number dependence of the cross section obtained from the present data was compared to that calculated by the eikonal approximation, as shown in Fig. 16(a). The

TABLE V. Inclusive (π^-, K^+) spectrum on C as a table. The quoted values of $-B_{\Sigma^-}$ are at the center of bins. Data in the region $82 \text{ MeV} < -B_{\Sigma^-} < 106 \text{ MeV}$ are omitted because of contamination by the events from H of the CH_2 target.

$-B_{\Sigma^-}$ (MeV)	$\bar{\sigma}_{4^\circ-8^\circ}$ ($\mu\text{b}/\text{sr}/\text{MeV}$)	Statistical errors	Systematic errors
-50.0	0.0103	0.0166	0.0005
-46.0	0.0286	0.0182	0.0097
-42.0	0.0052	0.0140	0.0003
-38.0	0.0181	0.0137	0.0011
-34.0	0.0614	0.0253	0.0032
-30.0	0.0514	0.0213	0.0021
-26.0	0.0225	0.0142	0.0008
-22.0	0.0496	0.0176	0.0021
-18.0	0.0318	0.0149	0.0014
-14.0	0.0641	0.0204	0.0039
-10.0	0.0497	0.0173	0.0034
-6.00	0.0388	0.0167	0.0013
-2.00	0.0584	0.0185	0.0021
2.000	0.0839	0.0224	0.0033
6.000	0.0518	0.0182	0.0047
10.00	0.0629	0.0200	0.0063
14.00	0.0716	0.0199	0.0033
18.00	0.1097	0.0257	0.0027
22.00	0.1482	0.0259	0.0041
26.00	0.1261	0.0251	0.0067
30.00	0.1610	0.0242	0.0066
34.00	0.1648	0.0260	0.0055
38.00	0.1636	0.0278	0.0064
42.00	0.2428	0.0320	0.0103
46.00	0.2912	0.0393	0.0173
50.00	0.3374	0.0375	0.0128
54.00	0.4634	0.0472	0.0135
58.00	0.5361	0.0539	0.0176
62.00	0.5040	0.0472	0.0279
66.00	0.6366	0.0561	0.0263
70.00	0.8127	0.0710	0.0459
74.00	0.7284	0.0659	0.0313
78.00	0.7202	0.0692	0.0289
82.00	0.0000	0.0000	0.0000
86.00	0.0000	0.0000	0.0000
90.00	0.0000	0.0000	0.0000
94.00	0.0000	0.0000	0.0000
98.00	0.0000	0.0000	0.0000
102.0	0.0000	0.0000	0.0000
106.0	0.0000	0.0000	0.0000
110.0	1.3992	0.1379	0.1062
114.0	1.3047	0.1430	0.1069
118.0	1.5827	0.1595	0.0559
122.0	1.4375	0.1480	0.0685
126.0	1.3142	0.1429	0.1314

TABLE V. (*Continued.*)

$-B_{\Sigma^-}$ (MeV)	$\bar{\sigma}_{4^\circ-8^\circ}$ ($\mu\text{b}/\text{sr}/\text{MeV}$)	Statistical errors	Systematic errors
130.0	0.7710	0.0995	0.1373
134.0	1.0794	0.1433	0.1063
138.0	0.9604	0.1549	0.0851
142.0	0.7663	0.1190	0.0555
146.0	1.0287	0.1507	0.1796
150.0	1.5495	0.2253	0.1189
154.0	1.2955	0.2376	0.5724
158.0	0.9786	0.2640	0.2432
162.0	0.7387	0.1783	0.0858
166.0	1.0623	0.5202	0.9010
170.0	0.4400	0.4218	0.8310
174.0	1.4755	0.5091	0.1655
178.0	0.8101	0.6703	0.5042
182.0	0.5911	0.8451	1.1040
186.0	0.6790	0.4109	0.2050
190.0	0.2408	0.3036	0.3022
194.0	0.3468	0.4105	0.2902
198.0	0.4235	0.3963	0.2496

horizontal axis is the target mass number, whereas the vertical axis is the ratio of the cross section as compared to the Si (Table IV). As can be seen in the figure, the mass-number dependence of the (π^-, K^+) reaction obtained from the present data shows a rather weak dependence compared to that found in a calculation by using the eikonal approximation. The present data were fitted by a function of $C_A \times A^\alpha$, where C_A is a constant and α is the fitting parameter. The value of α was found to be 0.20 ± 0.04 . Because α can reflect the effect of absorption, the present data show a stronger absorption than that from the eikonal approximation.

VI. COMPARISON WITH THE DISTORTED-WAVE IMPULSE APPROXIMATION CALCULATION

We calculated the inclusive (π^-, K^+) spectra within the framework of the distorted-wave impulse approximation (DWIA), and the calculated spectra were compared with the measured ones in order to obtain information on the Σ -nucleus potential. The formalism of the calculation can be found in the Appendix. In the calculation, we assumed the Woods-Saxon-type one-body potential for the Σ -nucleus potential, parametrized as

$$U(r) = (V_0 + iW_0)f(r) + V_{SO} \frac{\hbar^2}{(m_\pi c)^2} \frac{1}{r^2} \frac{df}{dr} (\ell \cdot \boldsymbol{\sigma}) + V_C(r), \quad (8)$$

$$f(r) = \frac{1}{1 + \exp[(r-c)/z]}, \quad (9)$$

where V_{SO} and V_C denote the spin-orbit and Coulomb potentials, respectively. The wave function of the initial nuclear

TABLE VI. Inclusive (π^-, K^+) spectrum on Ni as a table. The quoted values of $-B_{\Sigma^-}$ are at the center of bins.

$-B_{\Sigma^-}$ (MeV)	$\bar{\sigma}_{4^\circ-8^\circ}$ ($\mu\text{b}/\text{sr}/\text{MeV}$)	Statistical errors	Systematic errors
-50.0	0.0402	0.0238	0.0006
-46.0	0.0464	0.0228	0.0005
-42.0	0.0327	0.0199	0.0009
-38.0	0.0322	0.0198	0.0004
-34.0	0.0425	0.0206	0.0005
-30.0	0.0648	0.0261	0.0007
-26.0	0.0651	0.0234	0.0007
-22.0	0.0437	0.0223	0.0006
-18.0	0.0471	0.0207	0.0006
-14.0	0.1035	0.0240	0.0017
-10.0	0.0726	0.0226	0.0009
-6.0	0.0824	0.0234	0.0010
-2.0	0.0924	0.0226	0.0012
2.000	0.0837	0.0225	0.0009
6.000	0.0722	0.0205	0.0009
10.00	0.1197	0.0238	0.0014
14.00	0.1442	0.0248	0.0016
18.00	0.1342	0.0240	0.0016
22.00	0.1588	0.0248	0.0016
26.00	0.2233	0.0283	0.0025
30.00	0.1985	0.0268	0.0021
34.00	0.2382	0.0292	0.0026
38.00	0.3454	0.0333	0.0041
42.00	0.3787	0.0347	0.0049
46.00	0.4000	0.0355	0.0047
50.00	0.4529	0.0383	0.0077
54.00	0.5349	0.0407	0.0099
58.00	0.6191	0.0441	0.0154
62.00	0.6318	0.0441	0.0181
66.00	0.7529	0.0496	0.0290
70.00	0.8350	0.0500	0.0355
74.00	0.8329	0.0522	0.0403
78.00	0.9241	0.0609	0.0556
82.00	1.1104	0.0599	0.0686
86.00	1.2185	0.0635	0.0821
90.00	1.2426	0.0753	0.0761
94.00	1.3347	0.0689	0.0654
98.00	1.4305	0.0841	0.1260
102.0	1.4465	0.0887	0.1298
106.0	1.3691	0.0923	0.1248
110.0	1.4438	0.0879	0.1044
114.0	1.4801	0.1038	0.1194
118.0	1.4224	0.0983	0.1876
122.0	1.3406	0.1075	0.1183
126.0	1.4306	0.1707	0.1561
130.0	1.3283	0.1895	0.1368
134.0	1.5228	0.1890	0.2007

TABLE VI. (Continued.)

$-B_{\Sigma^-}$ (MeV)	$\bar{\sigma}_{4^{\circ}-8^{\circ}}$ ($\mu\text{b}/\text{sr}/\text{MeV}$)	Statistical errors	Systematic errors
138.0	1.3421	0.1820	0.2400
142.0	1.2459	0.1937	0.0881
146.0	1.1056	0.2547	0.2580
150.0	1.1761	0.3156	0.3438
154.0	1.2218	0.5745	0.4022
158.0	0.6356	0.3673	0.2316
162.0	0.9136	0.4570	0.1678
166.0	0.4536	0.4538	0.2631
170.0	0.9689	0.7014	0.2788

state was calculated with the Woods-Saxon-type potential of the same parametrization. To avoid any confusion, “Σ” is superscripted to the parameters, like V_0^{Σ} or W_0^{Σ} , if it is for the Σ-nucleus potential.

A. (π^- , K^+) spectrum on Si

We made a shape analysis of the (π^- , K^+) spectrum on Si, where the measured spectrum was fitted by the calculated ones for various Σ-nucleus potentials with the magnitude of each spectrum being a free parameter, as reported in Ref. [26]. We made an improvement in the calculation from those demonstrated in a previous report [26]; we took into account a much higher angular momentum transfer, up to 21, in the reaction, by which the magnitude of the (π^- , K^+) spectrum at higher $-B_{\Sigma^-}$ was increased. This caused a change in the fitting result from that obtained in the previous report [26]. Figure 17 shows the (π^- , K^+) spectrum on Si fitted by the calculated spectra. All of the data points (57 points) that appear in the figure are employed for the fitting. The potential parameters used for the calculation are the same as those in [26], as listed in the second column of Table X. Typical V_0^{Σ} and W_0^{Σ} dependences are shown in (a) and (b) in the figure. The spectrum shape shifts to a higher-excited region with an increase of V_0^{Σ} and is weakly dependent on W_0^{Σ} . The slopes of the calculated spectra with lower V_0^{Σ} just above $-B_{\Sigma^-}=0$ are relatively steep and thus do not reproduce the measured one. Particularly, the case of a shallow potential with $(V_0^{\Sigma}, W_0^{\Sigma}) = (-10 \text{ MeV}, -10 \text{ MeV})$, which was not excluded in the previous analysis in ^{12}C (stopped K^- , π^+) [42], is hard to reproduce the measured spectrum. Figure 18 shows a contour plot of the chi-square distribution. Here, the best-fit potential is found to be $(V_0^{\Sigma}, W_0^{\Sigma}) = (-110 \text{ MeV}, -45 \text{ MeV})$, where the chi square over the number of degree of freedom is $\chi^2/N_{\text{DOF}} = 29.48/56$. However, a wide region of V_0^{Σ} and W_0^{Σ} is still not excluded with respect to the confidence level. Therefore, the framework of the present theoretical analysis only demonstrates that (1) a strongly repulsive Σ-nucleus potential is required to reproduce the whole measured spectrum in shape, (2) an attractive potential is hard to reproduce the spectrum, and (3) the spectrum shape is not very sensitive to the imaginary potential, although a deep ($\sim -45 \text{ MeV}$) one seems to be favored.

TABLE VII. Inclusive (π^- , K^+) spectrum on In as a table. The quoted values of $-B_{\Sigma^-}$ are at the center of bins.

$-B_{\Sigma^-}$ (MeV)	$\bar{\sigma}_{4^{\circ}-8^{\circ}}$ ($\mu\text{b}/\text{sr}/\text{MeV}$)	Statistical errors	Systematic errors
-50.0	0.0855	0.0353	0.0039
-46.0	0.0587	0.0281	0.0017
-42.0	0.0035	0.0143	0.0002
-38.0	0.0499	0.0248	0.0009
-34.0	0.0302	0.0226	0.0022
-30.0	0.0415	0.0202	0.0021
-26.0	0.0329	0.0194	0.0010
-22.0	0.0490	0.0216	0.0021
-18.0	0.0814	0.0258	0.0121
-14.0	0.0724	0.0233	0.0030
-10.0	0.0763	0.0233	0.0058
-6.00	0.0860	0.0234	0.0035
-2.00	0.0650	0.0224	0.0014
2.000	0.0865	0.0247	0.0109
6.000	0.0846	0.0224	0.0055
10.00	0.1312	0.0275	0.0176
14.00	0.1349	0.0235	0.0097
18.00	0.1546	0.0264	0.0168
22.00	0.1861	0.0258	0.0062
26.00	0.2204	0.0327	0.0097
30.00	0.2731	0.0356	0.0168
34.00	0.3003	0.0370	0.0062
38.00	0.3572	0.0412	0.0063
42.00	0.4032	0.0442	0.0213
46.00	0.3974	0.0416	0.0091
50.00	0.5141	0.0476	0.0212
54.00	0.6095	0.0521	0.0124
58.00	0.7018	0.0558	0.0187
62.00	0.6084	0.0516	0.0155
66.00	0.7704	0.0586	0.0261
70.00	0.8492	0.0645	0.0564
74.00	0.8939	0.0662	0.0524
78.00	0.9444	0.0669	0.0824
82.00	1.1461	0.0755	0.0635
86.00	1.2693	0.0829	0.1165
90.00	1.3236	0.0901	0.1501
94.00	1.3309	0.0924	0.1541
98.00	1.5872	0.1001	0.1706
102.0	1.6932	0.1170	0.1890
106.0	1.6785	0.1125	0.1613
110.0	1.7317	0.1204	0.1089
114.0	1.4510	0.1092	0.1941
118.0	1.8136	0.1322	0.1464
122.0	1.8225	0.1271	0.1276
126.0	1.7817	0.1504	0.1325
130.0	1.7700	0.1312	0.1613
134.0	1.4876	0.1593	0.3185

TABLE VII. (*Continued.*)

$-B_{\Sigma^-}$ (MeV)	$\bar{\sigma}_{4^{\circ}-8^{\circ}}$ ($\mu\text{b}/\text{sr}/\text{MeV}$)	Statistical errors	Systematic errors
138.0	1.6231	0.1696	0.2132
142.0	1.8433	0.2599	0.2551
146.0	1.4337	0.2636	0.1433
150.0	1.1025	0.2401	0.4085
154.0	2.1866	0.5857	0.3323
158.0	1.4880	0.5633	0.2154
162.0	1.4392	0.7206	0.5350
166.0	3.8892	2.8229	0.9892
170.0	0.9020	0.2712	0.2883

Since the strength of the wave function outside the nucleus plays an important role in the magnitude of the inclusive spectrum in the repulsive Σ -nucleus potential, the potential radius is expected to be sensitive to the spectrum shape. Thus, we made another set of calculations with a radius parameter of $c=3.82$ fm and a depth of $V_0=-54.5$ MeV in the initial Si potential, as listed in the third column of Table X. The parameter $c=3.82$ fm was chosen to be $c \approx 1.26A^{1/3}$, which is close to the usually quoted radius parameter of the optical model. Fitted spectra are shown in typical cases of V_0^{Σ} and W_0^{Σ} in Fig. 19. Figure 20 shows a contour plot of the chi-square distribution. In this case, the best-fit potential is found to be $(V_0^{\Sigma}, W_0^{\Sigma})=(-90$ MeV, -40 MeV), where $\chi^2/N_{\text{DOF}}=27.33/56$. In Fig. 20, a good chi-square region becomes lower in the V_0^{Σ} axis, compared with Fig. 18. With this choice of potential parameters, we again demonstrate that a repulsive potential is required to reproduce the measured spectrum in shape, while an attractive potential is still hard to reproduce the spectrum. The spectrum shape is weakly sensitive to W_0^{Σ} . However, this result suggests that the choice of the potential radius parameter causes a systematic shift of the favored region in V_0^{Σ} and W_0^{Σ} .

B. Ni, In, and Bi

The fitting result in Si was applied to the other heavier targets. Figure 21 shows the calculated spectra with $(V_0^{\Sigma}, W_0^{\Sigma})=(90$ MeV, -40 MeV) fitted to the measured ones in Ni, In, and Bi. The other potential parameters are listed in Table X. The magnitude of the spectrum is arbitrarily adjusted, and all of the plotted data points in the figures were employed for the fitting. The values of χ^2/N_{DOF} in Ni, In, and Bi are 54.65/52, 33.51/53, and 37.55/48, respectively. The results show that the calculated spectra do not contradict the measured ones. We also applied a chi square test, as was done for Si. The fitting results show rather more repulsive potentials at the best chi square. However, it is unclear if the measured spectra maintain a sufficient sensitivity for a very repulsive potential greater than $V_0^{\Sigma} \sim 130$ MeV or so, since the data quality may decrease above $-B_{\Sigma} \sim 130$ MeV due to the limited acceptance of the spectrometer, as discussed in Sec. V. It is not very meaningful to discuss the importance of

TABLE VIII. Inclusive (π^-, K^+) spectrum on Bi as a table. The quoted values of $-B_{\Sigma^-}$ are at the center of bins.

$-B_{\Sigma^-}$ (MeV)	$\bar{\sigma}_{4^{\circ}-8^{\circ}}$ ($\mu\text{b}/\text{sr}/\text{MeV}$)	Statistical errors	Systematic errors
-50.0	0.0317	0.0257	0.0318
-46.0	0.0692	0.0383	0.0120
-42.0	0.0440	0.0260	0.0010
-38.0	0.0262	0.0214	0.0005
-34.0	0.0409	0.0300	0.0002
-30.0	0.0353	0.0195	0.0009
-26.0	0.0817	0.0339	0.0017
-22.0	0.0511	0.0238	0.0129
-18.0	0.0733	0.0295	0.0011
-14.0	0.0787	0.0256	0.0021
-10.0	0.0696	0.0236	0.0291
-6.00	0.0899	0.0317	0.0154
-2.00	0.0698	0.0247	0.0032
2.000	0.0680	0.0243	0.0086
6.000	0.1402	0.0296	0.0030
10.00	0.1323	0.0283	0.0029
14.00	0.1472	0.0292	0.0108
18.00	0.1893	0.0325	0.0033
22.00	0.2246	0.0385	0.0187
26.00	0.2397	0.0381	0.0112
30.00	0.2858	0.0397	0.0050
34.00	0.3895	0.0473	0.0114
38.00	0.4681	0.0538	0.0214
42.00	0.4490	0.0521	0.0250
46.00	0.5479	0.0567	0.0312
50.00	0.5748	0.0595	0.0378
54.00	0.6558	0.0635	0.0258
58.00	0.6803	0.0660	0.0222
62.00	0.9564	0.0791	0.0756
66.00	0.9413	0.0802	0.1025
70.00	1.0287	0.0865	0.0360
74.00	1.0385	0.0868	0.0627
78.00	1.3791	0.1059	0.1103
82.00	1.3769	0.1088	0.1643
86.00	1.4988	0.1157	0.1420
90.00	1.7458	0.1318	0.2109
94.00	1.6178	0.1326	0.2023
98.00	2.1074	0.1728	0.2810
102.0	2.1719	0.1984	0.1371
106.0	2.1885	0.2283	0.3826
110.0	1.6772	0.1956	0.4280
114.0	2.1402	0.1992	0.2697
118.0	2.2187	0.2057	0.0944
122.0	2.1832	0.2111	0.1191
126.0	2.3295	0.2213	0.2073
130.0	2.1486	0.2420	0.4238
134.0	2.7211	0.2151	0.5652

TABLE VIII. (Continued.)

$-B_{\Sigma^-}$ (MeV)	$\bar{\sigma}_{4^\circ-8^\circ}$ ($\mu\text{b}/\text{sr}/\text{MeV}$)	Statistical errors	Systematic errors
138.0	1.9433	0.3171	0.4770
142.0	2.0725	0.3910	0.3771
146.0	2.0192	0.6665	0.4241
150.0	2.3897	0.8487	0.2567
154.0	1.8168	0.7440	1.4051

the better chi squares compared to those obtained in cases of $(V_0^\Sigma, W_0^\Sigma) = (-90 \text{ MeV}, -40 \text{ MeV})$ because the χ^2 test only checks the inconsistency of the model. Therefore, we only demonstrate here that the repulsive potential obtained from the fitting analysis in Si is also applicable to the cases of Ni, In, and Bi.

C. (π^+, K^+) spectrum on C

We also applied the above-mentioned formalism to the inclusive (π^+, K^+) spectrum on ^{12}C at the same incident pion momentum of 1.2 GeV/c. In this case, the spectrum is dominated by the quasifree Λ production. Since the Λ -nucleus potential is well known, it is a good test to check if this formalism is applicable or not. The (π^+, K^+) spectrum on ^{12}C is plotted together with the calculated spectra in Fig. 22. The potential parameters used for the calculation are summarized in Table XI. The depth of the Λ -nucleus potential was taken to be $V_0^\Lambda = -30 \text{ MeV}$ (solid line). The spectrum for $V_0^\Lambda = 0 \text{ MeV}$ was also calculated for a comparison (dashed line). Many lambda hypernuclear states exist at around the lambda binding threshold and form a complicated structure in the spectral shape. More careful calculations on the relevant wave functions of the states, the width of the states, Gaussian convolution to simulate the experimental resolution (Lorentzian convolution in the present framework), and so on would be required to reproduce the spectrum much better in this region. Fractions of the $\Sigma^{0,+}$ productions contribute to the

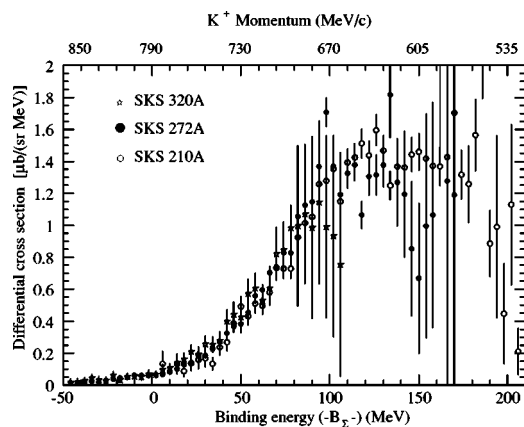


FIG. 9. Inclusive (π^-, K^+) spectrum on Si with three settings of the SKS current and with statistical errors only. The scattered kaon momentum is also depicted in the top of the figure.

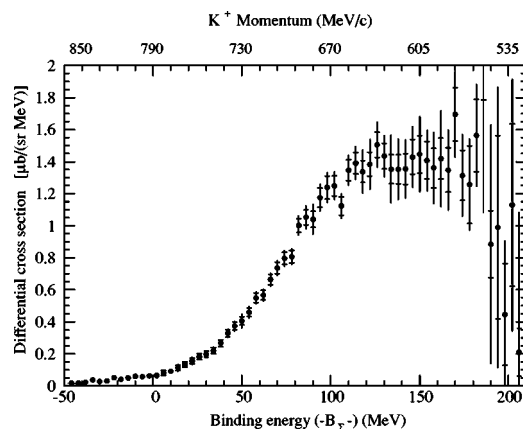


FIG. 10. Si spectrum obtained as a weighted average from three spectra measured with three SKS current settings. The quoted errors are both statistical and systematic, where the boundaries of the statistical errors are shown by arms and the systematic errors are drawn beyond the statistical errors.

spectrum above $-B_\Lambda \sim 80 \text{ MeV}$. For this reason, we avoided to apply the χ^2 -fitting test. The measured spectrum is thus overlaid with the calculated ones, where the magnitudes of which are arbitrarily adjusted by eye. The solid line reproduces the gross feature of the spectrum over a wide range of the Λ -binding energy.

VII. DISCUSSION

The measured spectra are characterized by gradually increasing the cross section along with an increase of $-B_{\Sigma^-}$ and the yield maximum at around $-B_{\Sigma^-}$ as high as 120 MeV, as mentioned in Sec. V. Within the present framework of the calculation, we obtain a repulsive Σ -nucleus potential to reproduce the measured spectra. A repulsive potential reduces the cross section at around the Σ^- -binding threshold and shifts the yield to a higher $-B_{\Sigma^-}$ region. In the present analysis, we took into account only the leading term in the inclusive (π^-, K^+) reaction. One can consider a multiple-scattering (multistep) process in the π^- incident, K^+

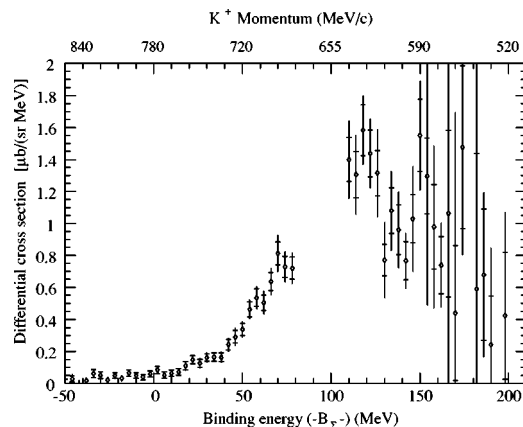


FIG. 11. Inclusive (π^-, K^+) spectrum on C from the CH_2 data. See the text for details.

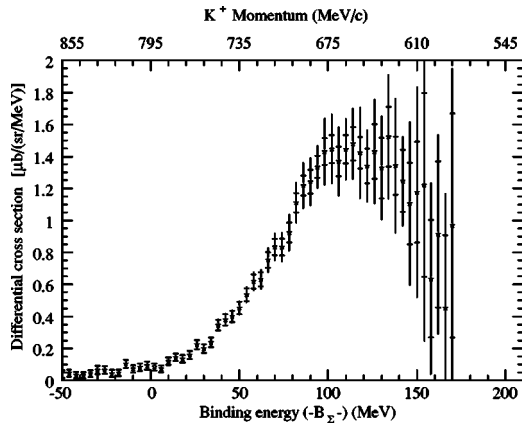


FIG. 12. Inclusive (π^- , K^+) spectrum on Ni.

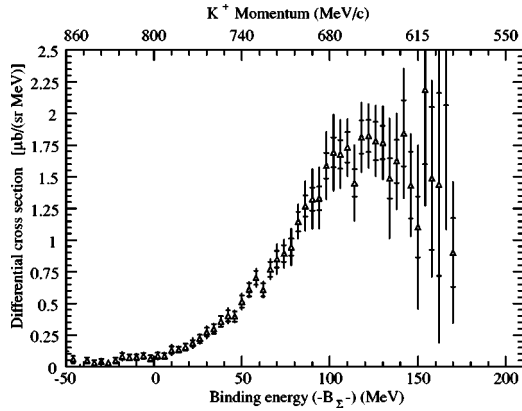


FIG. 13. Inclusive (π^- , K^+) spectrum on In.

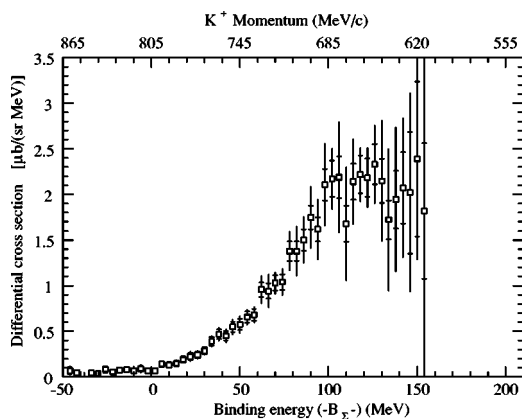


FIG. 14. Inclusive (π^- , K^+) spectrum on Bi.

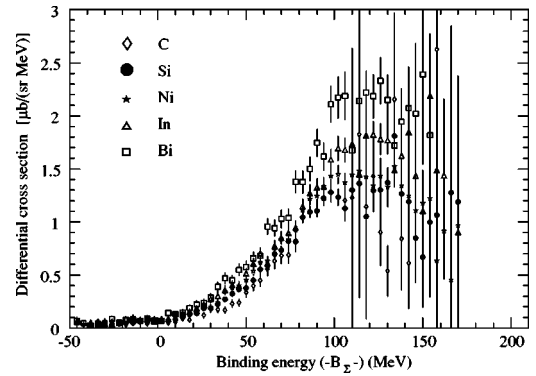


FIG. 15. Comparison of all the inclusive (π^- , K^+) spectra on each target taken with an SKS current setting of 272 A. The quoted errors are statistical only ones.

TABLE IX. Ratio of the cross section for each target as compared to the cross section on Si at an energy region of $0 < -B_{z^-} < 90$ MeV. The quoted errors are statistical.

Data	Ratio
C	0.81 ± 0.15
Si	1.0
Ni	1.16 ± 0.07
In	1.26 ± 0.09
Bi	1.49 ± 0.12

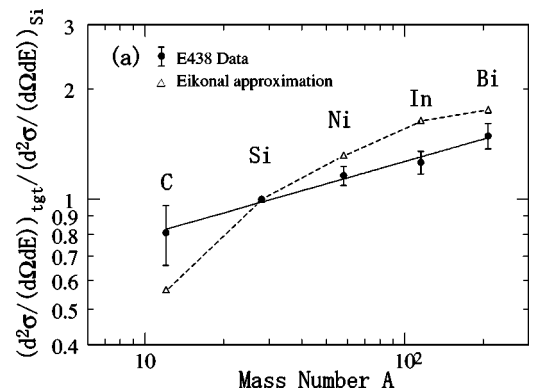


FIG. 16. Mass-number dependence of the cross section compared with the eikonal approximation. The quoted errors are only statistical ones.

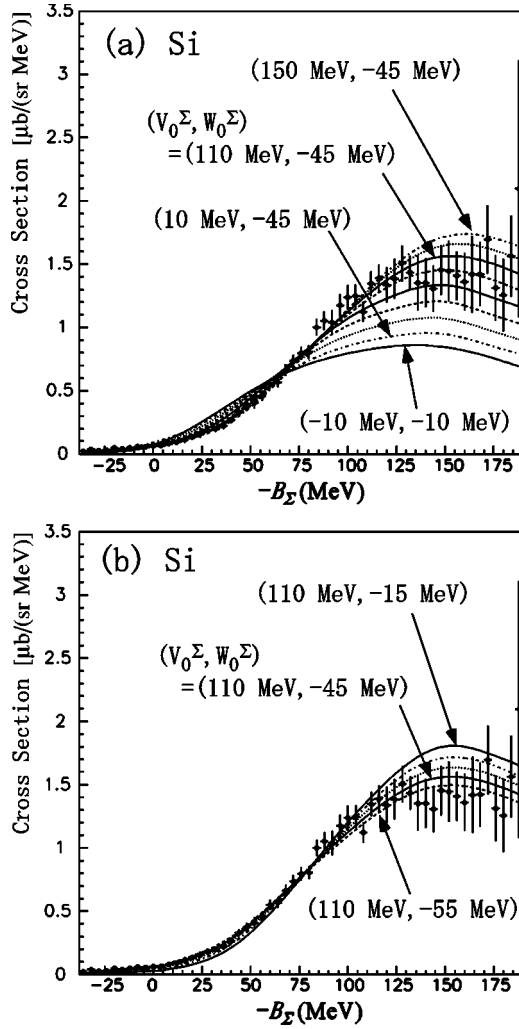


FIG. 17. Inclusive (π^- , K^+) spectrum on Si fitted by the calculated spectra. Typical V_0^Σ and W_0^Σ dependences are shown in (a) and (b). Curves in (a) are for $V_0^\Sigma=10-150$ MeV every 20 MeV fixing at $W_0^\Sigma=-45$ MeV except for the case of $(V_0^\Sigma, W_0^\Sigma)=(-10$ MeV, -10 MeV). Curves in (b) are for $W_0^\Sigma=-55$ to -15 MeV every 10 MeV fixing at $V_0^\Sigma=110$ MeV. The potential parameters used for the calculation are listed in the second column of Table X.

production reaction, which is expected to increase the yield at a higher $-B_\Sigma$. Although the effect of this multistep process is open for future studies, it might reduce the size of the repulsive potential to fit the measured spectra.

If the Σ -nucleus potential is repulsive, it is natural to interpret the yields in the Σ -bound region are due to a nonzero size of the imaginary potential, since these yields are beyond those expected from the Coulomb potential and those mixed by smearing with the experimental resolution. It is suggested that the imaginary potential is estimated to be $W_0^\Sigma \sim -12$ MeV or more by the standard expression $W_0^\Sigma \sim \Gamma/2 \sim -v\sigma_{av}\rho_p(0)/2$, where $(v\sigma_{av})$ denotes the Fermi averaging of the product of the relative velocity in ΣN and the $\Sigma N \rightarrow \Lambda N$ conversion cross section, and $\rho_p(0)$ is the proton density at the nuclear center [30]. This estimation is rather good for a low-energy ΣN interaction. For a higher-momentum ΣN interaction, as is expected in a large momentum-transfer

TABLE X. Potential parameters used for the DWIA calculation on the (π^- , K^+) reaction.

Parameter\target	^{28}Si	^{58}Ni	^{115}In	^{209}Bi	
U_Σ^a					
V_0 (MeV)	-10 to +150		+90		
W_0 (MeV)	-60 to -10		-40		
V_{SO} (MeV)		0			
c (fm) ^b	3.3	4.23	5.33	6.52	
z (fm)	0.67				
U_T^c					
V_0 (MeV) ^d	-49.6	-54.4	-51.6	-51.4	-55.5
W_0 (MeV)		0			
V_{SO} (MeV)		7			
c (fm) ^d	4.09	3.82	4.95	6.24	7.42
z (fm) ^e	0.536	0.517	0.563	0.468	

^a Σ -nucleus potential.

^b $c=1.1 \times (A-1)^{1/3}$.

^cProton single-particle potential of the initial nucleus.

^dThese are adjusted to reproduce the proton separation energy [27] and nuclear radius $\langle r^2 \rangle^{1/2}$ [28]. For Si, a smaller potential radius taken to be 3.82 fm was also calculated for comparison.

^eTaken from [28].

reaction (π^- , K^+) the imaginary potential may be deeper according to theoretical estimations [31,32], although this statement is still unclear, since the experimental data on the $\Sigma N \rightarrow \Lambda N$ cross section are limited at a higher momentum region.

Several sets of the hyperon-nucleon potential, based on the one-boson-exchange model, have been reported from the Nijmegen group [29]. There have been several attempts to calculate the Σ potential in nuclei and/or in nuclear matter using this two-body potential. Most of them gave rather attractive Σ potentials [31,33–36], but those with the Nijmegen model-F (NF) potential gave repulsive Σ -nucleus potentials [34,35]. The size of the repulsive potential was estimated to be $+3.6-8.1i$ MeV in nuclear matter by using NF [35]. They have reported the Σ -nucleus folding potentials in $^{28}\text{Si}-\Sigma$,

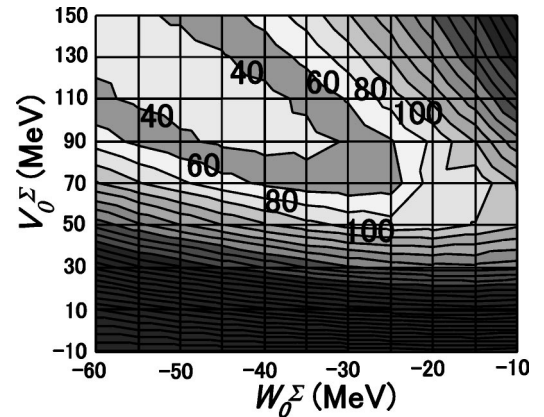


FIG. 18. Chi-square distribution in V_0^Σ and W_0^Σ for Si. The potential parameters used for the calculation are listed in the second column of Table X.

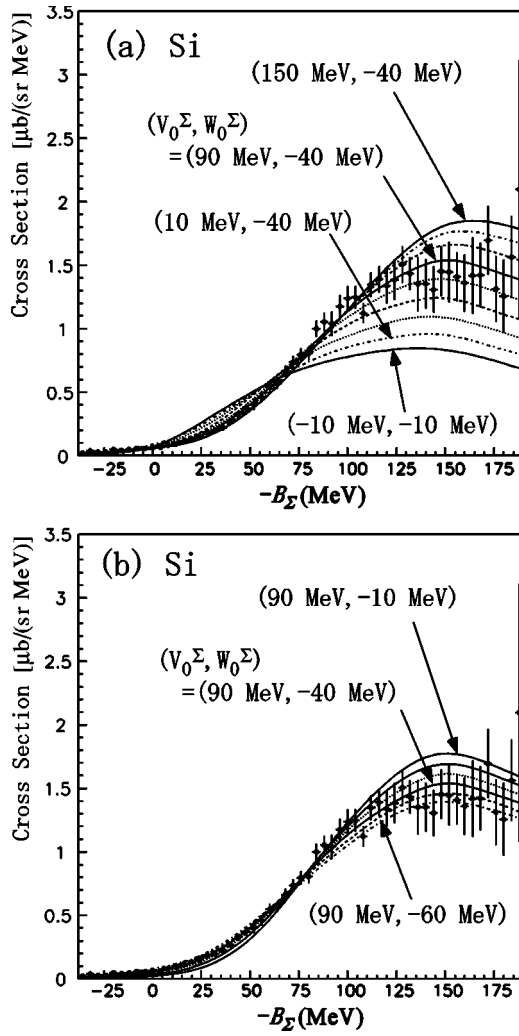


FIG. 19. Same as Fig. 17, but the curves in (a) are for $V_0^\Sigma = 10\text{--}150$ MeV every 20 MeV fixing at $W_0^\Sigma = -40$ MeV, except for the case of $(V_0^\Sigma, W_0^\Sigma) = (-10\text{ MeV}, -10\text{ MeV})$. Curves in (b) are for $W_0^\Sigma = -60$ to -10 MeV every 10 MeV fixing at $V_0^\Sigma = 90$ MeV. The potential parameters used for the calculation are listed in the third column of Table X.

based on the Nijmegen model-D (ND), F, and Softcore (NSC) YN potentials [35]. Among them, the ND-based potential is the most attractive, and the NSC-based one is weakly attractive. The NF-based potential has a repulsive core with a height ~ 30 MeV and an attractive pocket at the nuclear surface. The sizes of the imaginary potentials for ND, NF, and NSC are $W_0^\Sigma \sim -3.5$ MeV, -7.4 MeV, and -15 MeV. The Σ -nucleus potential suggested from the present measurement and the fitting analysis is more repulsive than those based on ND, NF, and NSC. A Σ single-particle potential has also been calculated [32] using the quark-model-based hyperon-nucleon interaction, model FSS proposed by the Kyoto-Niigata group [37]. The Σ potential turns out to be 20.4 MeV repulsive, since the $\Sigma N(I=3/2) {}^3S_1$ state shows a strongly repulsive nature due to the Pauli-exclusion effect between the quarks.

A repulsive Σ -nucleus potential has been derived so as to reproduce the Σ^- -atomic x-ray data by employing a phenom-

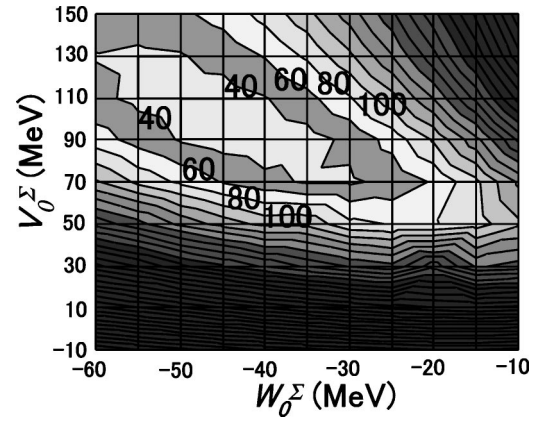


FIG. 20. Same as Fig. 18, but the potential parameters used for the calculation are listed in the third column of Table X.

enological density-dependent (DD) potential [38,39] or the relativistic mean-field (RMF) theory [39]. The DD potential shows a strongly repulsive core having a height of ~ 95 MeV at the nuclear center with a shallow attractive tail outside of the nucleus; the imaginary potential is as deep as $W_0^\Sigma \sim -35$ MeV. The RMF approach was used to construct a Schrödinger-equivalent Σ -nucleus potential from the scalar (attractive) and vector (repulsive) Dirac potentials, while fitting the experimental Σ^- -atomic x-ray shift and width. This approach shows a change of the Σ -nucleus potential from attractive to repulsive in the nuclear interior along with an increase of α_ω from $1/3$ to 1 , where α_ω is the vector-meson coupling ratio. The fitting is better when α_ω increases. In the case of Si, the real and imaginary potentials are, respectively, about 30–40 MeV and as deep as 40 MeV in the nuclear interior. The Σ -nucleus potential derived by fitting the Σ^- -atomic data seems qualitatively close to that obtained from the present analysis of the (π^-, K^+) spectra. However, the calculated Si (π^-, K^+) spectrum with the DD potential within the present framework did not fit the measured spectrum very well, as shown in Fig. 23. This does not show that the volume of the DD potential is strongly repulsive. Since the x-ray data suggest an attractive potential in the atomic orbital region, the present Woods-Saxon-type repulsive potential does not reproduce the x-ray data. Therefore, further studies of the Σ -nucleus potential would be required to explain the present measurements and the x-ray data, where more careful choices of the nuclear and Σ -nuclear radii and the figure of the Σ -nucleus potential at the nuclear surface and outside the nucleus would be necessary.

The hyperon constituents of neutron star cores are closely related to the hyperon single-particle potential in dense nuclear matter and hence are discussed based on the results from hypernuclear studies [13,15,36,40]. However, discussions concerning hyperons other than Λ are ambiguous, particularly for Σ , because the interactions of the hyperon to nucleon and other hyperons are not well established. The Σ^- appearance in dense neutron matter is sometimes discussed based on an attractive Σ -nucleus potential in nuclear matter of normal density [13,15,40]. On the other hand, the hyperon mixing in dense neutron matter is discussed based on the repulsive Σ -nucleus potential derived from the Σ^- -atomic

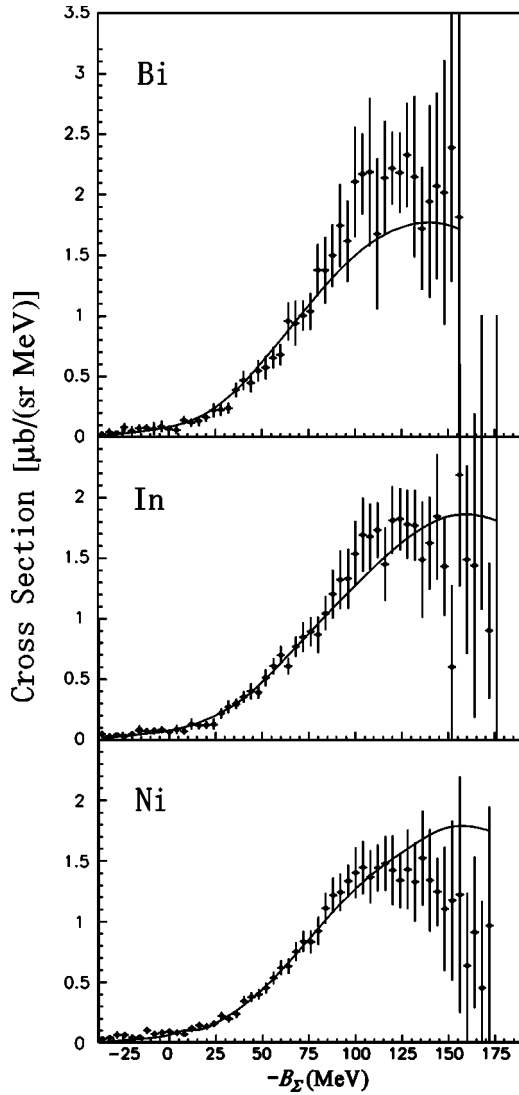


FIG. 21. Inclusive (π^- , K^+) spectra on Ni, In, and Bi fitted by the calculated spectra with $(V_0^\Sigma, W_0^\Sigma) = (90 \text{ MeV}, -40 \text{ MeV})$. The other potential parameters used for the calculations are listed in the fourth to the sixth columns of Table X.

x-ray data in [13]. In this regard, the repulsive Σ -nucleus potential from the present result should be taken into account for discussing the hyperon dynamics in neutron-star cores.

VIII. SUMMARY AND CONCLUSIONS

In the present experiment, we measured the inclusive (π^- , K^+) spectra for the first time on several medium-to-heavy nuclear targets (C, Si, Ni, In, and Bi) with reasonable statistics. The calibration of the horizontal axis (B_{Σ^-}) was done successfully with a precision of better than $\pm 0.1 \text{ MeV}$; also the angular distribution of the measured elementary cross section well reproduced previous bubble-chamber data, indicating a reliability of the measured cross section. The energy resolution was obtained to be $3.31 \pm 0.33 \text{ MeV}$ (FWHM). All spectra show a similarity in shape, at least at an energy region of $0 < -B_{\Sigma^-} < 90 \text{ MeV}$; also the mass-

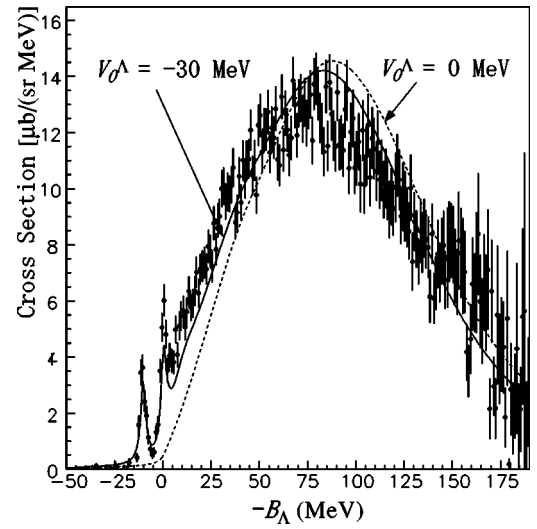


FIG. 22. Inclusive (π^+ , K^+) spectrum on C is shown. The solid and dashed lines are calculated spectra with $V_0^\Lambda = -30 \text{ MeV}$ and 0 MeV , respectively.

number dependence of the cross section was found to be rather weaker than that from the eikonal approximation.

We performed a DWIA calculation of the inclusive (π^+ , K^+) spectra on Si, Ni, In, and Bi, for various depths (heights) of the Woods-Saxon-type, one-body Σ -nucleus potential and compared it with the measured ones concerning the shape. The present analysis demonstrated that a repulsive Σ -nucleus potential having a nonzero size of the imaginary part is required to reproduce the observed spectra. However, further studies on the Σ -nucleus potential, particularly choices of the nuclear and Σ -nuclear radii and the details of the potential shape at the nuclear surface and outside the nucleus, would be required in order to explain both the present measurements and the x-ray data.

TABLE XI. Potential parameters used for the DWIA calculation on the (π^- , K^+) reaction.

	Λ -nucleus potential		Initial C
	U_Λ	U_Λ^{0a}	U_T^b
V_0 (MeV)	-30	0	-50.3 ^c
W_0 (MeV)	0 ^d	0 ^d	0 ^e
V_{SO} (MeV)	1	1	7
c (fm)	2.45 ^f	2.45 ^f	3.15 ^c
z (fm)	0.6	0.6	0.51

^a U_Λ^{0a} was calculated for a comparison.

^bNeutron single-particle potential of the initial nucleus (C).

^cThese are adjusted to reproduce the neutron separation energy (18.731 MeV) [27] and nuclear radius $\langle r^2 \rangle^{1/2} = 2.454 \text{ fm}$ [28].

^dA constant value of -1.5 MeV was added to the imaginary potential to simulate the experimental energy resolution.

^eA constant value of -6 MeV was added to the imaginary potential for the s -nucleon hole state.

^f $c = 1.1 \times (A - 1)^{1/3}$.

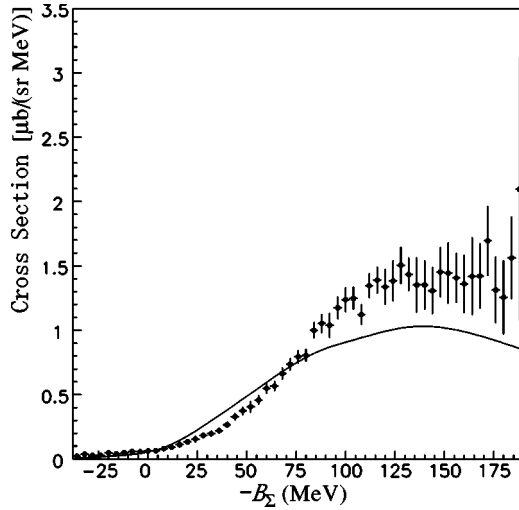


FIG. 23. Inclusive (π^- , K^+) spectrum on Si fitted by the calculated spectrum with the DD potential.

ACKNOWLEDGMENTS

The authors are grateful to Professor Y. Akaishi, Professor T. Harada, and Dr. T. Koike for many invaluable discussions and inspiring comments in the analysis stage of the present experiment. They also thank Dr. R. E. Chrien for proofreading this article. They would like to express their sincere gratitude to Professor K. Nakamura, the head of KEK Physics division III, and Professor Yoshimura, former coordinator of EPPC (Experimental planning and Program Coordination), for their encouragement and extended helping hands to perform the present experiment. They greatly thank to all staff members of KEK-PS as well as the accelerator and the beam channel group members for delivering a stable proton beam. A stable operation of the SKS system by Y. Kakiguchi is also highly appreciated. Indispensable support from the Counter-Experimental Hall group, Online/Electronics, and Cryogenics groups is also greatly appreciated. One of the authors, P.K.S., was supported by the JSPS (Japan Society for the Promotion of Science) (Grant No. P01186).

APPENDIX: DWIA CALCULATION FORMALISM

A distorted-wave impulse approximation has often been used to evaluate the cross sections of the hypernuclear states in (K^- , π^\pm), (π^\pm , K^+), and others. The Morimatsu-Yazaki formalism has been successfully applied to an analysis of the (K^- , π^\pm) spectra in helium [41] and carbon [42]. It has also been applied to the (π^- , K^+) reaction. The cross section of the inclusive reaction can be written as

$$\frac{d^2\sigma}{d\Omega dE} = \beta \left(\frac{d\sigma}{d\Omega_{el}} \right) S(E), \quad (\text{A1})$$

where β is the kinematical factor for a coordinate transfer from a two-body system to a many-body system [45], and $d\sigma/d\Omega_{el}$ represents the averaged differential cross section of the elementary reaction. Here, the elementary cross section

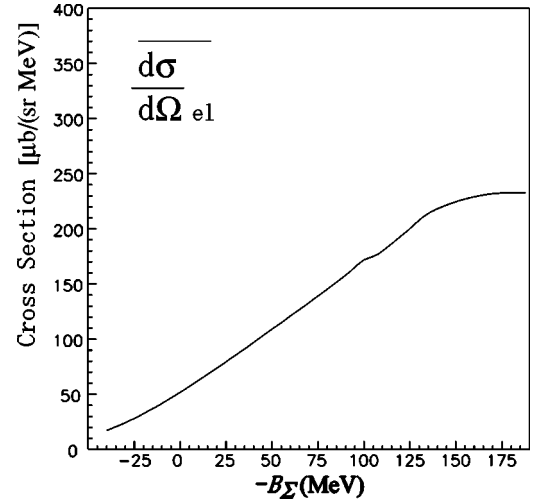


FIG. 24. Fermi-averaged elementary $p(\pi^-, K^+)\Sigma^-$ cross section $d\sigma/d\Omega_{el}$, as a function of $-B_{\Sigma^-}$ in Si.

$[d\sigma/d\Omega(s, \Omega_K)]$ is averaged over the momentum of a proton (\mathbf{k}) moving in the target nucleus with a weight of the momentum distribution $[\rho(\mathbf{k})]$, written as

$$\frac{d\sigma}{d\Omega_{el}}(E) = \frac{\int \rho(\mathbf{k}) \frac{d\sigma}{d\Omega}(s, \Omega_K) \delta(k - P) dk}{\int \rho(\mathbf{k}) \delta(k - P) dk}, \quad (\text{A2})$$

$$P = k_{K^+} + k_{\Sigma^-} - k_{\pi^-}. \quad (\text{A3})$$

The delta function is required for energy-momentum conservation in the elementary reaction. Relevant particles are treated on mass shell, and the possible \mathbf{k} is given by k_{π^-} and k_{K^+} at $E(-B_{\Sigma^-})$. As a result, $d\sigma/d\Omega_{el}$ depends on E . Figure 24 shows calculated $d\sigma/d\Omega_{el}$ as a function of $-B_{\Sigma^-}$ in Si. In this calculation, the elementary (π^-, K^+) reaction cross section $d\sigma/d\Omega(s, \Omega_K)$ was taken from Refs. [25,43], where s is the Mandelstam variable. The momentum distribution of a bound nucleon $\rho(\mathbf{k})$ was given by the single-particle wave function of the hole state. For the elementary (π^+, K^+) reaction, $d\sigma/d\Omega(s, \Omega_K)$ was calculated by using the parameters obtained from the partial wave analysis [44]. The obtained $d\sigma/d\Omega_{el}$ in Fig. 24 reflects the fact that the elementary (π^-, K^+) cross section increases when s is smaller at a forward-scattering angle in the laboratory frame. This energy dependence is important to explain the spectrum shape. Particularly, the (π^+, K^+) spectrum shape cannot be reproduced without taking this energy dependence into account.

The strength function $[S(E)]$ is written as

$$S(E) = -\frac{1}{\pi} \text{Im} \sum_{\alpha\alpha'} \int d\mathbf{r} d\mathbf{r}' f_{\alpha}^{\dagger}(\mathbf{r}) G_{\alpha\alpha'}(E; \mathbf{r}', \mathbf{r}) f_{\alpha'}(\mathbf{r}'), \quad (\text{A4})$$

$$f_{\alpha}(\mathbf{r}) = \chi^{(-)*}(\mathbf{R}) \chi^{(+)}(\mathbf{R}) \langle \alpha | \psi_N(\mathbf{r}) | i \rangle, \quad (\text{A5})$$

$$\mathbf{R} = (M_c/M_{hy})\mathbf{r}. \quad (\text{A6})$$

Here, f_α is the form factor characterized by the distorted waves of the incident and outgoing particles ($\chi^{(+)}$ and $\chi^{(-)}$) and the nucleon-hole state [$\langle \alpha | \psi_N(\mathbf{r}) | i \rangle$]. The recoil effect of the residual nucleus is taken into consideration in Eq. (A6). The response function can be described by means of the Green's function [cf Eq. (2.2) in Ref. [46]]. Here, we assume the Woods-Saxon-type one-body Σ-nucleus potential [$U_\Sigma(r) = V_0^\Sigma(r) + iW_0^\Sigma(r)$]. Then, the Green's function (G) becomes diagonal and is a solution of

$$[E + \hbar^2/(2\mu)\Delta - U(\mathbf{r})]G(E; \mathbf{r}', \mathbf{r}) = -\delta(\mathbf{r}' - \mathbf{r}), \quad (\text{A7})$$

$$U(\mathbf{r}) = U_\Sigma(\mathbf{r}) + U_C(\mathbf{r}), \quad (\text{A8})$$

where μ is the reduced mass and U_C represents the Coulomb potential. Then, neglecting the off-diagonal couplings, the partial wave decomposition of $S(E)$ can be expressed as

$$S(E) = \sum_{JM} \sum_{l_Y j_Y n_N l_N j_N} \sum W(j_N, J_Y, J) S_{l_Y j_Y n_N l_N j_N}^{JM}(E), \quad (\text{A9})$$

where

$$W(j_N, J_Y, J) = (2j_N + 1) \left(j_N \frac{1}{2} J 0 \middle| j_Y \frac{1}{2} \right)^2 \quad (\text{A10})$$

for the closed shell and

$$\begin{aligned} S_{l_Y j_Y n_N l_N j_N}^{JM}(E) = & -\frac{1}{\pi} \int dr dr' r^2 r'^2 [\tilde{J}_{JM}^*(p_\pi, p_K, \theta_K, r) \phi_{n_N l_N j_N}^*(r) \\ & \times G_{l_Y j_Y n_N l_N j_N}^J(E; r', r) \tilde{J}_{JM}(p_\pi, p_K, \theta_K, r') \\ & \times \phi_{n_N l_N j_N}(r')]. \end{aligned} \quad (\text{A11})$$

Here, $\phi_{n_N l_N j_N}$ represents a radial wave function of a nucleon-hole state, and \tilde{J}_{JM} is defined by the partial-wave decomposition of the distorted waves, written as

$$\chi^{(-)*}(p_K, \mathbf{R}) \chi^{(+)}(p_\pi, \mathbf{R}) = \sum_{JM} \tilde{J}_{JM}(p_\pi, p_K, \theta_K, r) Y_J^M(\Omega). \quad (\text{A12})$$

The partial-wave decomposition of the Green's function, $G^J \equiv G_{l_Y j_Y n_N l_N j_N}^J$, is a solution of the following equation:

$$\begin{aligned} \left[\frac{\hbar^2}{2\mu} \left(\frac{d^2}{dr^2} + \frac{2}{r} \frac{d}{dr} - \frac{\ell(\ell+1)}{r^2} \right) + E - U(r) \right] G^J(E; r', r) \\ = -\frac{1}{r^2} \delta(r' - r), \end{aligned} \quad (\text{A13})$$

where G^J is generally expressed as

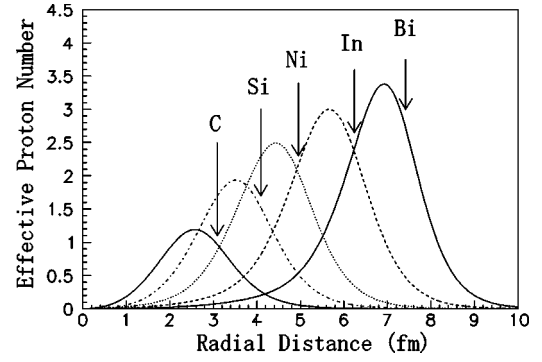


FIG. 25. Calculated radial distributions of the effective proton numbers [$D_{eff}(r)$] of the (π^-, K^+) reactions on C, Si, Ni, In, and Bi. Solid (smaller one), dotted, dashed, and solid (larger one) curves are those for C, Si, Ni, In, and Bi, respectively. Arrows indicate positions of the nuclear radii.

$$G^J = A y_1(r_{<}) y_2(r_{>}). \quad (\text{A14})$$

Here, y_1 and y_2 are the regular and outgoing solutions of the differential equation, the left-hand side of Eq. (A13) equals 0, and $r_{<}(r_{>})$ means the smaller (larger) one of r and r' . The factor A is normalized so as to satisfy $A(y_2 y_1' - y_1 y_2') = (2\mu)/(\hbar r)^2$.

Distorted waves of the pion and kaon were calculated using the eikonal approximation, assuming $\sigma_{\pi-N} = 35$ mb and $\sigma_{K^+N} = 14$ mb [47]. As described in Ref. [47], we calculated the effective nucleon number (N_{eff}) as

$$N_{eff} = \int D_{eff}(r) dr, \quad (\text{A15})$$

$$D_{eff}(r) = \int \rho(r) |\chi^{(-)*}(p_K, \mathbf{R})|^2 |\chi^{(+)}(p_\pi, \mathbf{R})|^2 r^2 d\Omega, \quad (\text{A16})$$

where $\rho(r)$ represents the nucleon density distribution. Figure 25 shows calculated radial distributions of the effective proton numbers [$D_{eff}(r)$] of the (π^-, K^+) reactions on C, Si, Ni, In, and Bi. This figure indicates how much the (π^-, K^+) reaction penetrates into the nuclear interior. The distortion reduces the magnitude of the spectrum. As described in Sec. V, the measured distortion seems to be stronger than that expected from the eikonal approximation. The absolute strength of the distortion is still unclear. The strength of the distortion does not affect the spectrum shape very much. Thus, the magnitude of the spectrum is arbitrarily adjusted with a free parameter in the present spectrum shape analysis.

- [1] P. H. Pile *et al.*, Phys. Rev. Lett. **66**, 2585 (1991).
 [2] T. Hasegawa *et al.*, Phys. Rev. C **53**, 1210 (1996).
 [3] H. Hotchi *et al.*, Phys. Rev. C **64**, 044302 (2001).
 [4] D. J. Millener *et al.*, Phys. Rev. C **38**, 2700 (1988).
 [5] H. Tamura *et al.*, Phys. Rev. Lett. **84**, 5963 (2000).
 [6] H. Akikawa *et al.*, Phys. Rev. Lett. **88**, 082501 (2002).
 [7] R. Bertini *et al.*, Phys. Lett. **90B**, 375 (1980).
 [8] R. Sawfta, Nucl. Phys. **A545**, 103c (1995).
 [9] T. Nagae *et al.*, Phys. Rev. Lett. **80**, 1605 (1998).
 [10] S. Bart *et al.*, Phys. Rev. Lett. **83**, 5238 (1999).
 [11] R. S. Hayano *et al.*, Phys. Lett. B **231**, 355 (1989).
 [12] T. Harada, S. Shinmura, Y. Akaishi, and H. Tanaka, Nucl. Phys. **A507**, 715 (1990).
 [13] S. Balberg and A. Gal, Nucl. Phys. **A625**, 435 (1997).
 [14] T. Takatsuka, Y. Yamamoto, and R. Tamagaki, Int. J. Mod. Phys. B **15**, 1609 (2001), and references therein.
 [15] M. Baldo, G. F. Burgio, and H.-J. Schulze, Phys. Rev. C **58**, 3688 (1998).
 [16] H. Noumi *et al.*, KEK-PS-Proposal No. E438, 1998.
 [17] H. Bandō, T. Motoba, and J. Žofka, Int. J. Mod. Phys. A **5**, 4032 (1990).
 [18] T. Fukuda *et al.*, Nucl. Instrum. Methods Phys. Res. A **361**, 485 (1995).
 [19] J. Myrheim *et al.*, Nucl. Instrum. Methods **160**, 43 (1979).
 [20] D. E. Groom *et al.*, Eur. Phys. J. C **15**, 1 (2000).
 [21] P. K. Saha, Ph.D. thesis, Sokendai, KEK Report. 2001-17, 2001.
 [22] T. Hasegawa, Ph.D. thesis, University of Tokyo, 1994.
 [23] H. Hotchi, Ph.D. thesis, University of Tokyo, 2000.
 [24] CERN Program Library Entry W5013, Computer code GEANT.
 [25] M. L. Good *et al.*, Phys. Rev. **183**, 1142 (1969).
 [26] H. Noumi *et al.*, Phys. Rev. Lett. **89**, 072301 (2002); **90**, 049902 (2003).
 [27] *Table of Isotopes*, 8th ed., edited by R. B. Firestone *et al.* (Wiley, New York, 1996).
 [28] H. de Vries *et al.*, At. Data Nucl. Data Tables **36**, 495 (1987).
 [29] M. M. Nagels, Th. A. Rijken, and J. J. de Swart, Phys. Rev. D **12**, 744 (1975); **15**, 2547 (1977); **20**, 1633 (1979); P. Maessen, Th. A. Rijken, and J. J. de Swart, Phys. Rev. C **40**, 2226 (1989); Th. A. Rijken, V. G. J. Stoks, and Y. Yamamoto, *ibid.* **59**, 21 (1999).
 [30] A. Gal and C. B. Dover, Phys. Rev. Lett. **44**, 379 (1980); **44**, 962 (1980).
 [31] H.-J. Schulze, M. Baldo, U. Lombardo, J. Cugnon, and A. Lejeune, Phys. Rev. C **57**, 704 (1998).
 [32] M. Kohno, Y. Fujiwara, T. Fujita, C. Nakamoto, and Y. Suzuki, Nucl. Phys. **A674**, 229 (2000).
 [33] J. Dąbrowski and J. Rożnek, Phys. Rev. C **23**, 1706 (1981); W. Stepień-Rudzka and S. Wycech, Nucl. Phys. **A362**, 349 (1981); R. Brockmann and E. Oset, Phys. Lett. **118B**, 33 (1982); Y. Yamamoto and H. Bandō, Prog. Theor. Phys. **73**, 905 (1985); M. Kohno, *ibid.* **78**, 123 (1987); D. Halderson, Phys. Rev. C **40**, 2173 (1989); K. S. Myint, S. Tadokoro, and Y. Akaishi, Prog. Theor. Phys. **82**, 112 (1989); S. Tadokoro and Y. Akaishi, Phys. Rev. C **42**, 2591 (1990); M. Kohno, Prog. Theor. Phys. **88**, 537 (1992).
 [34] Y. Yamamoto and H. Bandō, Prog. Theor. Phys. **69**, 1312 (1983).
 [35] T. Yamada and Y. Yamamoto, Prog. Theor. Phys. Suppl. **117**, 241 (1994).
 [36] Y. Yamamoto, S. Nishizaki, and T. Takatsuka, Prog. Theor. Phys. **103**, 981 (2000).
 [37] Y. Fujiwara, C. Nakamoto, and Y. Suzuki, Phys. Rev. Lett. **76**, 2242 (1996); Phys. Rev. C **54**, 2180 (1996).
 [38] C. J. Batty, E. Friedman, and A. Gal, Prog. Theor. Phys. Suppl. **117**, 227 (1994).
 [39] J. Mareš, E. Friedman, A. Gal, and B. K. Jennings, Nucl. Phys. **A594**, 311 (1995).
 [40] J. Schaffner and I. N. Mishustin, Phys. Rev. C **53**, 1416 (1996).
 [41] T. Harada, Nucl. Phys. **A672**, 181 (2000).
 [42] M. Iwasaki, Ph.D. thesis, University of Tokyo, 1987; R. S. Hayano, Nucl. Phys. **A478**, 113c (1988); H. Tamura *et al.*, *ibid.* **A479**, 161c (1988); H. Ota, T. Yamazaki, M. Iwasaki, and R. S. Hayano, Prog. Theor. Phys. Suppl. **117**, 177 (1994).
 [43] O. I. Dahl *et al.*, Phys. Rev. **163**, 1430 (1967); J. C. Doyle *et al.*, *ibid.* **165**, 1483 (1968).
 [44] M. Sotona and J. Žofka, Prog. Theor. Phys. **81**, 160 (1989).
 [45] S. Tadokoro, H. Kobayashi, and Y. Akaishi, Phys. Rev. C **51**, 2656 (1995).
 [46] O. Morimatsu and K. Yazaki, Nucl. Phys. **A483**, 493 (1988).
 [47] C. B. Dover, L. Ludeking, and G. E. Walker, Phys. Rev. C **22**, 2073 (1980).